
Improved damp heat and thermal cycling stability of organic solar cells

In the format provided by the authors and unedited

Table-of-contents

Supplementary Notes 1-5

Supplementary Figures 1-39

Supplementary Tables 1-14

Supplementary Notes

Supplementary Note 1. Method to measure the T_g and T_{onset} .

For the T_g test of active layer films we refer to the approach in the literature by Samuel et al.¹ We measure the thermal transition by the shift in the UV-Vis absorption spectrum that occurs in the films after thermal annealing. This shift is often attributed to the formation of ordered aggregates and is often accompanied by an improvement in the charge transport properties of the films. Once the annealing temperature exceeds the transition temperature, there is a significant change in the absorption spectrum. For quantitative analysis we use the deviation metric (DM_T), which is the sum of the squared deviations of the absorbance.

$$DM_T = \sum_{\lambda_{min}}^{\lambda_{max}} [I_{RT}(\lambda) - I_T(\lambda)]^2 \quad (1)$$

where $I_{RT}(\lambda)$ and $I_T(\lambda)$ are the absorption intensities of the as-cast (room temperature) and annealed films, respectively, λ is the wavelength, and λ_{min} and λ_{max} are the lower and upper bounds of the optical sweep, respectively.

To identify the temperature at which the film begins to change, we differentiate the deviation metric with respect to temperature after fitting the data to a smooth curve and define the temperature at which the change begins to occur as the T_{onset} , which is used as the basis for screening the stabilised active layer films.

Supplementary Note 2. Calculation of overall activation energy (E_a) based on the Arrhenius model

Based on the experimental data, we quantified the activation energy of performance degradation by applying the Arrhenius model from the temperature-dependent acceleration factor².

$$k_{deg} = A \exp\left(-\frac{E_a}{k_B T}\right) \quad (2)$$

where E_a is the activation energy for thermal degradation, k_B is the Boltzmann constant, T is the temperature, and A is the pre-exponential factor. The reaction rate coefficient k_{deg} was obtained by combining linear degradation kinetics with experimental data.

The degradation acceleration factor K was extracted from the ratio of degradation rate constants at different temperatures

$$K = \frac{k_{deg'}}{k_{deg}} = \exp\left[\frac{E_a}{k_B} \left(\frac{1}{T} - \frac{1}{T'}\right)\right] \quad (3)$$

We calculated the E_a of devices based on the CMA structure of the PM6:BO-4Cl:PC₆₁PeA system using the Arrhenius model. We fitted a linear degradation to the normalised efficiency for the devices heated at 85 °C and 150 °C for 1000 h (Supplementary Figure 26). The degradation rate was $2.25 \times 10^{-3} \% \text{ h}^{-1}$ at 85 °C and $3 \times 10^{-2} \% \text{ h}^{-1}$ at 150 °C, giving a calculated E_a of 0.52 eV. Using the acceleration factor, the degradation rate at 45°C (expected operation temperature of solar cells) was predicted to be $2.71 \times 10^{-4} \% \text{ h}^{-1}$, the T80 lifetime of 25.2 years was achieved (assuming an average of 8 h of operation per day).

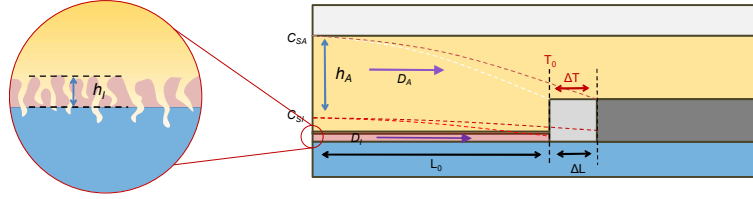
Supplementary Note 3. Method of testing and calculating the adhesion of aluminium foil butyl tapes.

The adhesion of the aluminium foil butyl tape is tested using an electronic universal testing machine (MTS Exceed E44, MTS Systems Co., Ltd.). The tape was cut into strips 2 cm wide and 10 cm long, with one end bonded to the glass substrate. A tensile peel test was performed on the universal testing machine at a peel angle of 180° and a tensile speed of 400 mm/min.

The calculation of adhesion force is based on the peel force and the width of the tape. The peel force is the maximum force with which the tape can be peeled from the substrate. The equation is expressed as

$$\textit{Adhesion Force} = \frac{\textit{Peel Force}}{\textit{Width of the Tape}} \quad (4)$$

Supplementary Note 4. Derivation of equations for a model of calcium corrosion by lateral diffusion of water vapor.



In the water vapor lateral diffusion model, we use calcium corrosion and Fick's second law to establish the lateral diffusion equation for water vapor. We assume that (1) the thickness of the Ca film is thin enough that the absorption of water by the Ca film does not affect the kinetic process of water vapor diffusion. (2) The reaction between Ca and water is fast enough that water above the Ca film can be quickly reacted with the Ca without further diffusion.

At any moment, the corrosion contribution to Ca consists of two parts, the adhesive layer (bulk diffusion) as well as the interface layer (interface diffusion), and the contributions of the two parts can be calculated independently. Assuming that water vapor diffusion processes through the adhesive layer and interface follow the well-developed Fick- model. For the one-dimensional (1D) case, Fick's second law is expressed as:

$$\frac{\partial C}{\partial t} = D \frac{\partial^2 C}{\partial x^2} \quad (5)$$

Where C is the concentration of the diffusing substance, D is the diffusion coefficient of the substance, x is the diffusion distance, and t is the diffusion time.

The concentration distribution of water vapor can be expressed as a Gaussian error function:

$$C(x, t) = C_S \left(1 - \operatorname{erf} \left(\frac{x}{2\sqrt{Dt}} \right) \right) \quad (6)$$

Where C_S is the saturation concentration of the substances in the medium.

The concentration equations for these two layers can be described as:

$$C_A(x, t) = C_{SA} \left(1 - \operatorname{erf} \left(\frac{x}{2\sqrt{D_A t}} \right) \right) \quad (7)$$

$$C_I(x, t) = C_{SI} \left(1 - \operatorname{erf} \left(\frac{x}{2\sqrt{D_I t}} \right) \right) \quad (8)$$

Where C_{SA} and C_{SI} are the saturation water vapor concentration at the adhesion and the interface, D_A and D_I represent the diffusion constants of water vapor through the adhesive and the interface, respectively.

Then in a time difference (ΔT) of calcium boundary moves from L_0 to $L_0 + \Delta L$ the total amount of water vapor that corrodes the calcium (in $\text{mol} \cdot \text{m}^{-1}$) can be calculated to be:

$$N_{H_2O} = \Delta L N_0 = \frac{2\Delta L h_{Ca} \rho_{Ca}}{M_{Ca}} \quad (9)$$

Where h_{Ca} is the thickness of the calcium film, ρ_{Ca} is the density of calcium, M_{Ca} is the molar mass of calcium.

In the meanwhile, the total amount of water vapor reaching the calcium edge through the bulk adhesive (J_A) and the interface (J_I) (in $\text{mol} \cdot \text{m}^{-1}$) during the time period ΔT can be calculated to be:

$$J_A = \int_{L_0+\Delta L}^{\infty} h_A C_A(x, T_0 + \Delta T) dx - \int_{L_0}^{\infty} h_A C_A(x, T_0) dx \quad (10)$$

$$J_I = \int_{L_0+\Delta L}^{\infty} h_I C_I(x, T_0 + \Delta T) dx - \int_{L_0}^{\infty} h_I C_I(x, T_0) dx \quad (11)$$

Where h_A is the thickness of the adhesive layer and h_I is the thickness of the interface layer.

Thus volume diffusion and interfacial diffusion of water vapor can be expressed as respectively:

$$J_A = C_{SA} h_A \int_{L_0+\Delta L}^{\infty} \left(1 - \text{erf} \left(\frac{x}{2\sqrt{D_A(T_0+\Delta T)}}\right)\right) dx - C_{SA} h_A \int_{L_0}^{\infty} \left(1 - \text{erf} \left(\frac{x}{2\sqrt{D_A T_0}}\right)\right) dx \quad (12)$$

$$J_I = C_{SI} h_I \int_{L_0+\Delta L}^{\infty} \left(1 - \text{erf} \left(\frac{x}{2\sqrt{D_I(T_0+\Delta T)}}\right)\right) dx - C_{SI} h_I \int_{L_0}^{\infty} \left(1 - \text{erf} \left(\frac{x}{2\sqrt{D_I T_0}}\right)\right) dx \quad (13)$$

Since calcium corrosion comes only from the water vapor erosion, the total amount of water vapor for calcium corrosion should be equal to the total amount of water vapor passing through the bulk adhesive and the interface, i.e.:

$$N_{H_2O} = J_A + J_I \quad (14)$$

From Eqs. (12), (13) and (14):

$$\begin{aligned} \Delta L N_0 = & C_{SA} h_A \int_{L_0+\Delta L}^{\infty} \left(1 - \text{erf} \left(\frac{x}{2\sqrt{D_A(T_0+\Delta T)}}\right)\right) dx - C_{SA} h_A \int_{L_0}^{\infty} \left(1 - \text{erf} \left(\frac{x}{2\sqrt{D_A T_0}}\right)\right) dx + \\ & C_{SI} h_I \int_{L_0+\Delta L}^{\infty} \left(1 - \text{erf} \left(\frac{x}{2\sqrt{D_I(T_0+\Delta T)}}\right)\right) dx - C_{SI} h_I \int_{L_0}^{\infty} \left(1 - \text{erf} \left(\frac{x}{2\sqrt{D_I T_0}}\right)\right) dx \end{aligned} \quad (15)$$

The relationship between the diffusion distance x and the diffusion time t of water vapor during diffusion is given by:

$$x = K\sqrt{t} \quad (16)$$

Where K is defined as the apparent diffusion rate.

From Eq. (16), we can know:

$$K\sqrt{T_0 + \Delta T} = L_0 + \Delta L \quad (17)$$

$$K\sqrt{T_0} = L_0 \quad (18)$$

From Eqs. (17) and (18) we can get:

$$\sqrt{T_0 + \Delta T} = \frac{L_0 + \Delta L}{L_0} \sqrt{T_0} \quad (19)$$

Substitution of Eq. (19) into Eqs. (12) and (13):

$$J_A = \frac{2\Delta L\sqrt{D_A T_0}}{L_0} C_{SA} h_A \int_{\frac{L_0}{2\sqrt{D_A T_0}}}^{\infty} \operatorname{erfc}(y) dy \quad (20)$$

$$J_I = \frac{2\Delta L\sqrt{D_I T_0}}{L_0} C_{SI} h_I \int_{\frac{L_0}{2\sqrt{D_I T_0}}}^{\infty} \operatorname{erfc}(y) dy \quad (21)$$

Hence Eq. (15) becomes:

$$N_0 = \frac{2\sqrt{D_A T_0}}{L_0} C_{SA} h_A \int_{\frac{L_0}{2\sqrt{D_A T_0}}}^{\infty} \operatorname{erfc}(y) dy + \frac{2\sqrt{D_I T_0}}{L_0} C_{SI} h_I \int_{\frac{L_0}{2\sqrt{D_I T_0}}}^{\infty} \operatorname{erfc}(y) dy \quad (22)$$

As

$$\int_{\frac{L_0}{2\sqrt{D_A T_0}}}^{\infty} \operatorname{erfc}(y) dy = \frac{e^{-\left(\frac{L_0}{2\sqrt{D_A T_0}}\right)^2}}{\sqrt{\pi}} - \frac{L_0}{2\sqrt{D_A T_0}} \operatorname{erfc}\left(\frac{L_0}{2\sqrt{D_A T_0}}\right) \quad (23)$$

Solving the Eqs. (20) and (21) leads to:

$$J_A = \frac{2\sqrt{D_A T_0}}{L_0} C_{SA} h_A \left(\frac{e^{-\left(\frac{L_0}{2\sqrt{D_A T_0}}\right)^2}}{\sqrt{\pi}} - \frac{L_0}{2\sqrt{D_A T_0}} \operatorname{erfc}\left(\frac{L_0}{2\sqrt{D_A T_0}}\right) \right) \quad (24)$$

$$J_I = \frac{2\sqrt{D_I T_0}}{L_0} C_{SI} h_I \left(\frac{e^{-\left(\frac{L_0}{2\sqrt{D_I T_0}}\right)^2}}{\sqrt{\pi}} - \frac{L_0}{2\sqrt{D_I T_0}} \operatorname{erfc}\left(\frac{L_0}{2\sqrt{D_I T_0}}\right) \right) \quad (25)$$

Substituting Eqs. (24) and (25) into Eq. (22) yields:

$$N_0 = \frac{2\sqrt{D_A T_0}}{L_0} C_{SA} h_A \left(\frac{e^{-\left(\frac{L_0}{2\sqrt{D_A T_0}}\right)^2}}{\sqrt{\pi}} - \frac{L_0}{2\sqrt{D_A T_0}} \operatorname{erfc}\left(\frac{L_0}{2\sqrt{D_A T_0}}\right) \right) + \frac{2\sqrt{D_I T_0}}{L_0} C_{SI} h_I \left(\frac{e^{-\left(\frac{L_0}{2\sqrt{D_I T_0}}\right)^2}}{\sqrt{\pi}} - \frac{L_0}{2\sqrt{D_I T_0}} \operatorname{erfc}\left(\frac{L_0}{2\sqrt{D_I T_0}}\right) \right) \quad (26)$$

Substituting Eq. (18) into Eq. (26) and collating gives:

$$h_A = \frac{K \left(N_0 - \frac{2\sqrt{D_I}}{K} C_{SI} h_I \left(\frac{e^{-\left(\frac{K^2}{4D_I}\right)}}{\sqrt{\pi}} - \frac{K}{2\sqrt{D_I}} \operatorname{erfc}\left(\frac{K}{2\sqrt{D_I}}\right) \right) \right)}{2\sqrt{D_A} C_{SA} \left(\frac{e^{-\left(\frac{K^2}{4D_A}\right)}}{\sqrt{\pi}} - \frac{K}{2\sqrt{D_A}} \operatorname{erfc}\left(\frac{K}{2\sqrt{D_A}}\right) \right)} \quad (27)$$

Considering $\sqrt{D_I} \gg K$, Eq. (27) can be reduced to

$$h_A = \frac{K \left(N_0 - \frac{2\sqrt{D_I}}{K} C_{SI} h_I \frac{1}{\sqrt{\pi}} \right)}{2\sqrt{D_A} C_{SA} \left(\frac{e^{-\left(\frac{K^2}{4D_A}\right)}}{\sqrt{\pi}} - \frac{K}{2\sqrt{D_A}} \operatorname{erfc}\left(\frac{K}{2\sqrt{D_A}}\right) \right)} \quad (28)$$

For ease of calculation and fitting to the experimental data, Eq. (28) has been simplified using a first-order approximation of the Taylor expansion:

$$h_A = \frac{K \left(N_0 - \frac{2\sqrt{D_I}}{K} C_{SI} h_I \frac{1}{\sqrt{\pi}} \right)}{2\sqrt{D_A} C_{SA} \left(\frac{1}{\sqrt{\pi}} + \frac{K^2}{4\sqrt{\pi} D_A} - \frac{K}{2\sqrt{D_A}} \right)} \quad (29)$$

Supplementary Note 5. Accurate calculation of the encapsulation edge width of the device.

In a square encapsulation layer, the presence of two-dimensional diffusion results in corners being corroded earlier. The water vapor diffusion rate is fastest along the diagonal direction. Based on experiments and simulations we obtained that the apparent diffusion rate K_{diag} at the diagonal is in fixed proportion to the apparent diffusion rate K_{edge} at the edge, with an empirical value of about 1.54, i.e:

$$\frac{K_{diag}}{K_{edge}} \approx 1.54 \quad (30)$$

It can be obtained from the relationship between the diffusion distance and diffusion time of water vapor:

$$x_{diag} = K_{diag}\sqrt{t} \quad (31)$$

Where x_{diag} is the distance that water vapor moves diagonally from one corner of the encapsulation layer to the corresponding corner of the device.

Thus the edge width of the encapsulation layer can be calculated from the geometric relationship:

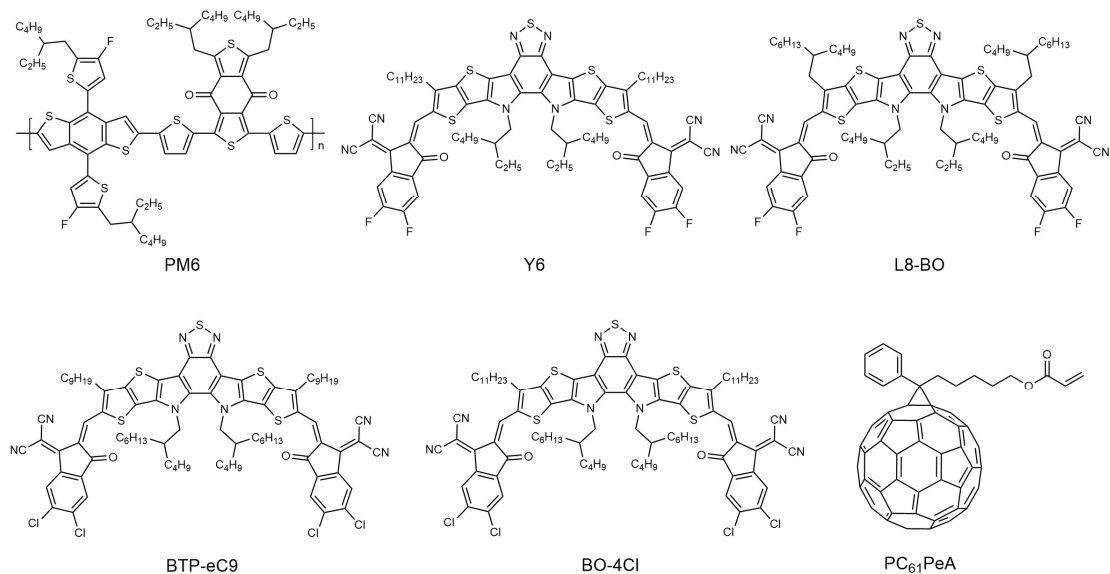
$$x_{diag} = \sqrt{2}x_{edge} \quad (32)$$

Combining Eqs. (30), (31) and (32) gives:

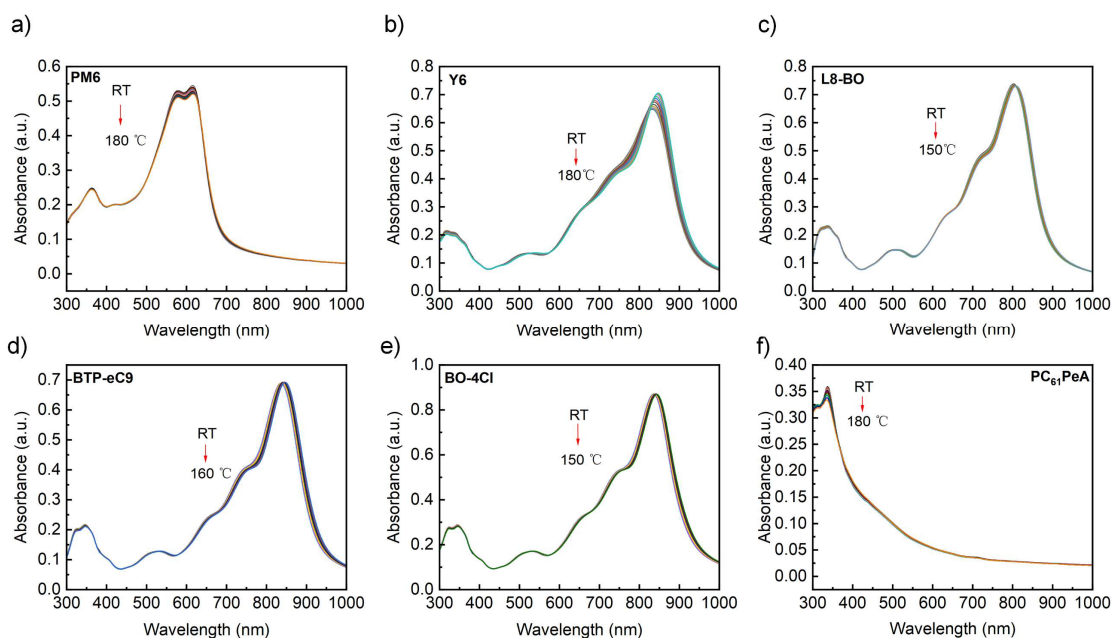
$$x_{edge} \approx 1.09 K_{edge}\sqrt{t} \quad (33)$$

In ABT encapsulant encapsulation, the apparent water vapor diffusion rate at the edge can be minimized in the double 85 test at $1.1 \times 10^{-5} \text{ m/s}^{1/2}$ when the annealing temperature is 80°C and the thickness of the adhesive layer is 200 μm . In order to protect the device from corrosion for 1000 hours under the double 85 condition, the required edge width can be calculated to be at least 22.7 mm using Eq. (33).

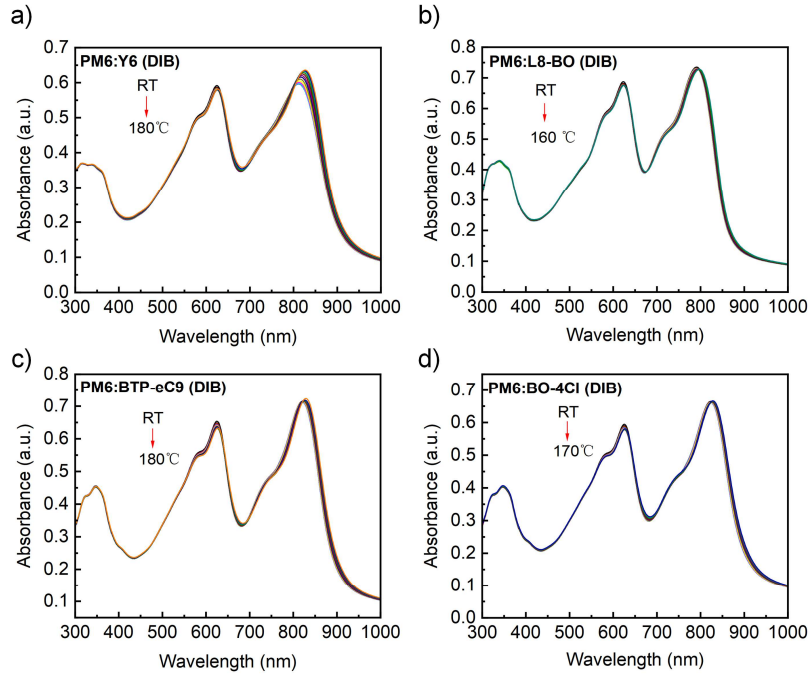
Supplementary Figures



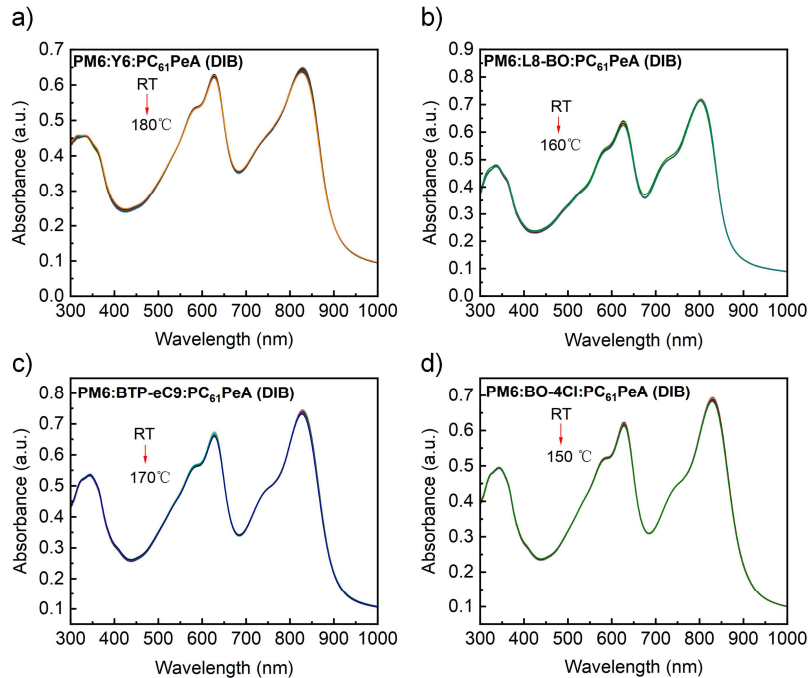
Supplementary Figure 1. Molecular structures of the organic semiconductors used in this study. Molecular structures of PM6, Y6, L8-BO, BTP-eC9, BO-4Cl and PC₆₁PeA.



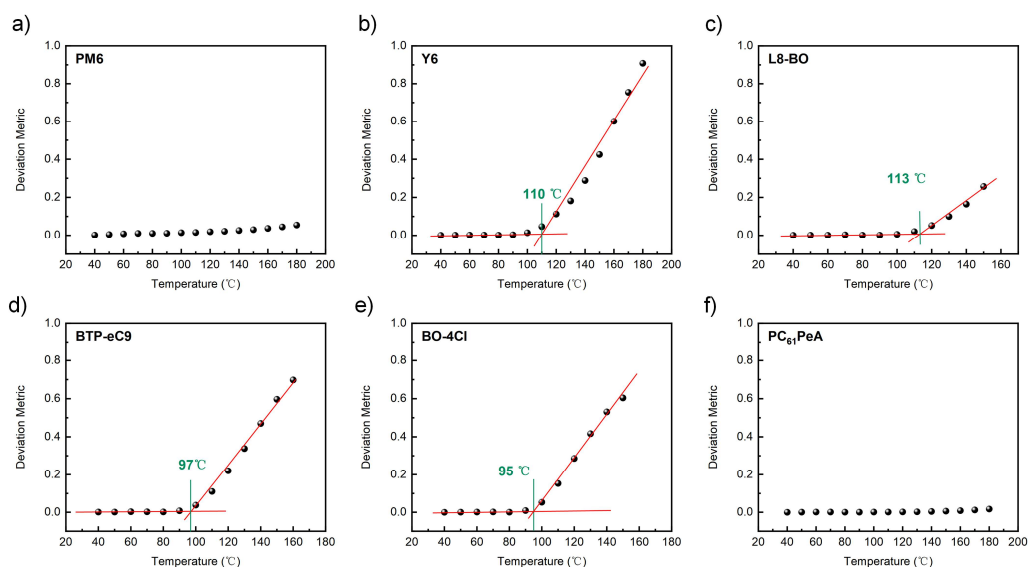
Supplementary Figure 2. UV-Vis absorption spectrum of single-component films. UV-Vis absorption spectra of PM6, Y6, L8-BO, BTP-eC9, BO-4Cl and PC₆₁PeA films annealed at different temperatures for 5min.



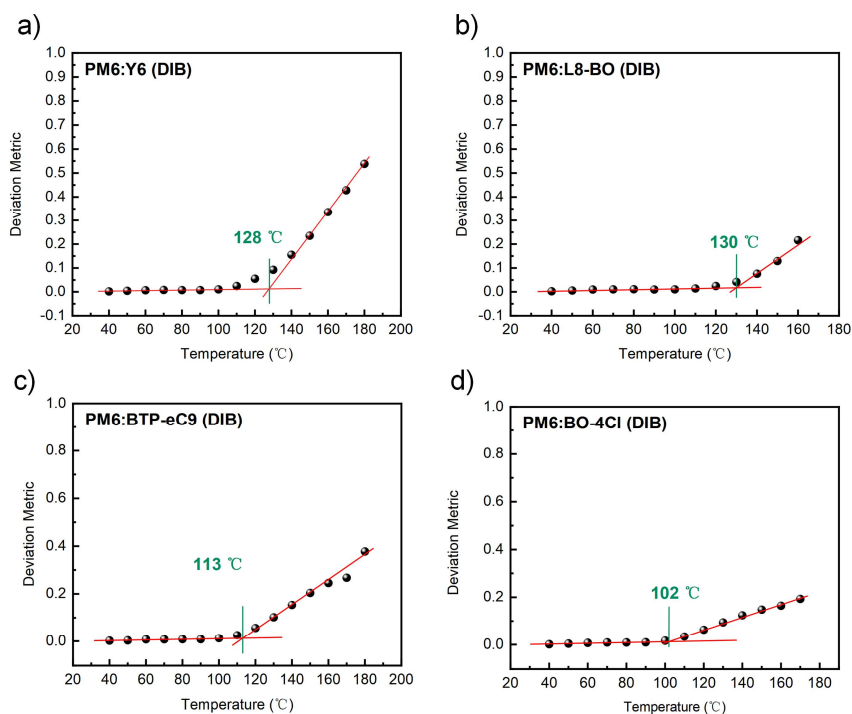
Supplementary Figure 3. UV-Vis absorption spectrum of binary films. UV-Vis absorption spectra of binary blend films with PM6 as donor and Y6, L8-BO, BTP-eC9, BO-4Cl as acceptors, respectively, annealed at different temperatures for 5 min.



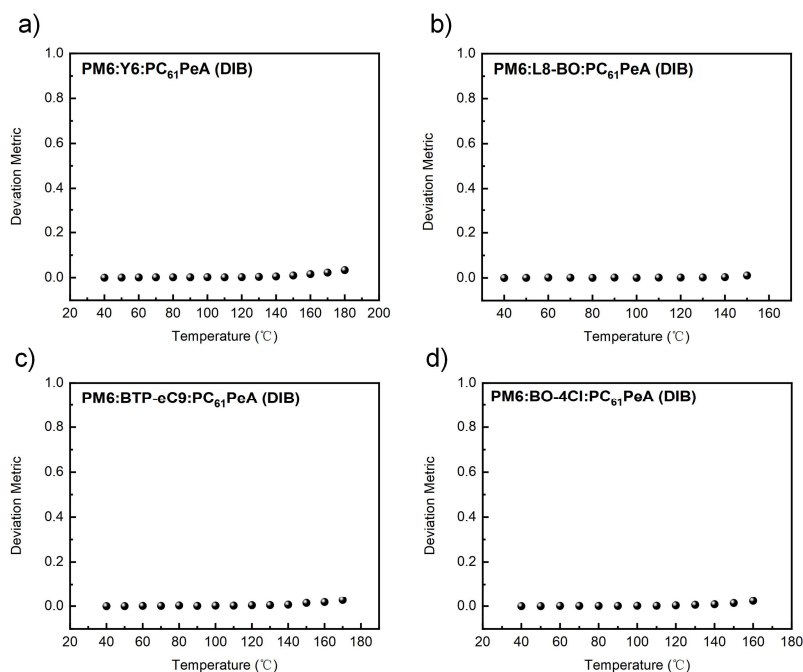
Supplementary Figure 4. UV-Vis absorption spectrum of ternary films. UV-Vis absorption spectra of ternary blend films with PM6 as the donor, Y6, L8-BO, BTP-eC9, BO-4Cl as the acceptors, respectively, and PC₆₁PeA as the third component, annealed at different temperatures for 5 min.



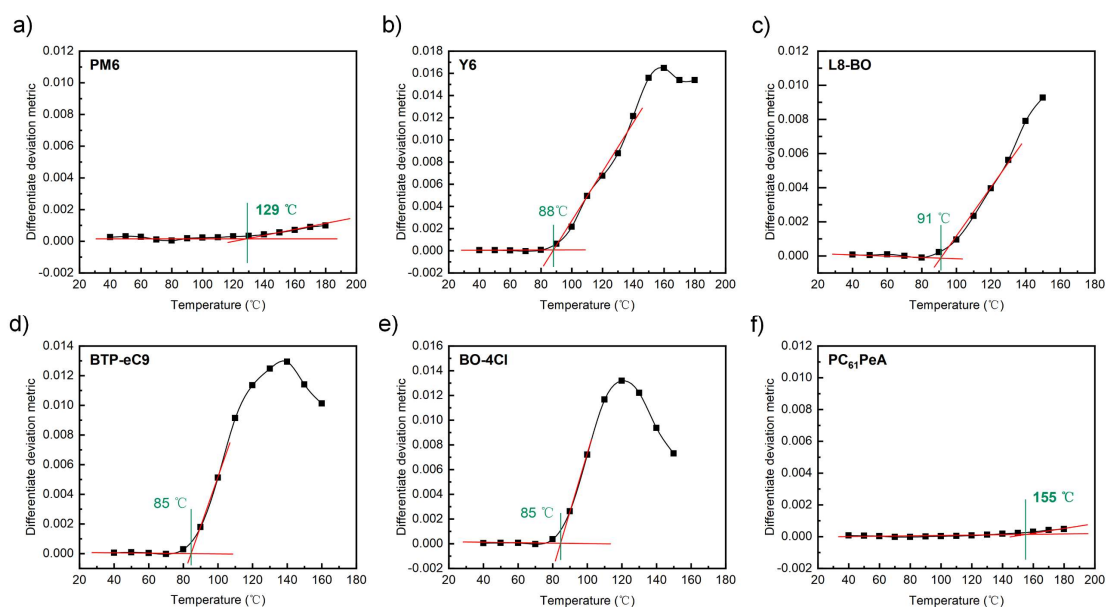
Supplementary Figure 5. Deviation metrics of UV-Vis absorption spectra of single-component films at different temperatures. Deviation metrics of UV-Vis absorption spectra of PM6, Y6, L8-BO, BTP-eC9, BO-4Cl and PC₆₁PeA films annealed at different temperatures for 5 min with respect to the as-cast (room temperature) conditions. The curves are obtained by segmented linear fitting.



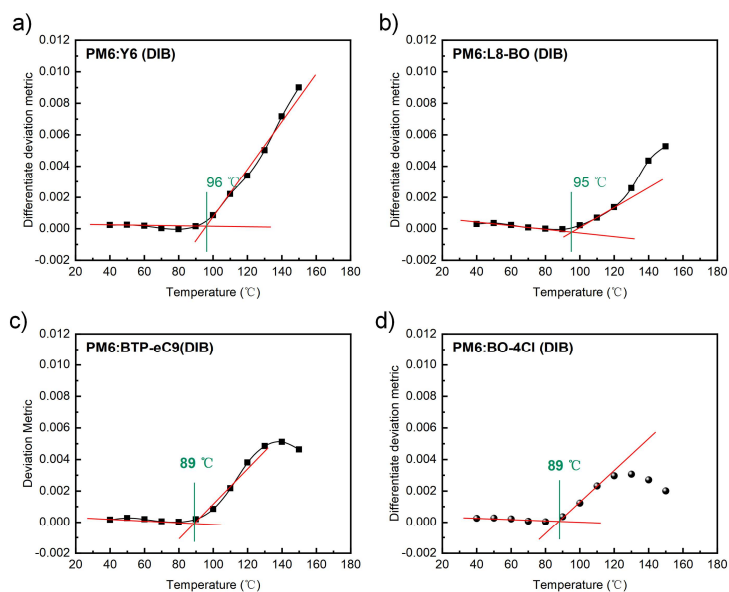
Supplementary Figure 6. Deviation metrics of UV-Vis absorption spectra of binary films at different temperatures. Deviation metrics of UV-Vis absorption spectra of binary blended films with PM6 as donor and Y6, L8-BO, BTP-eC9, BO-4Cl as acceptors, respectively, annealed for 5 min at different temperatures with respect to the as-cast (room temperature) conditions. The curves are obtained by segmented linear fitting.



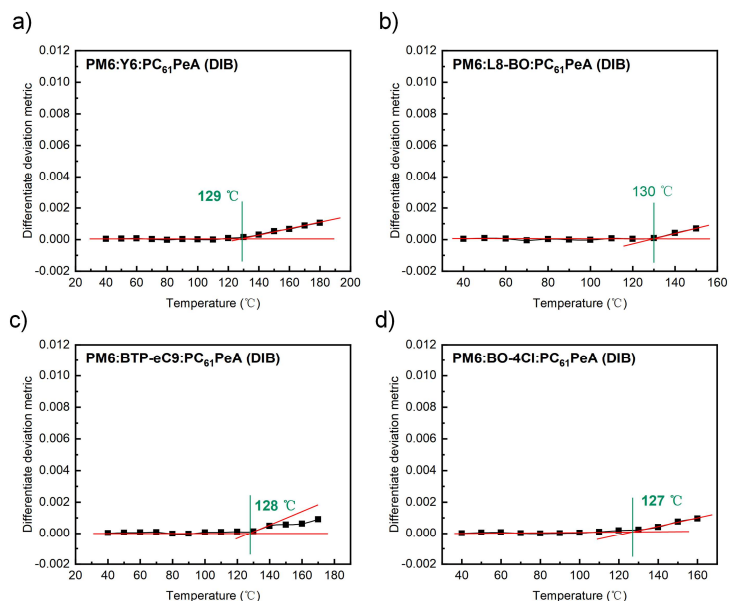
Supplementary Figure 7. Deviation metrics of UV-Vis absorption spectra of ternary films at different temperatures. Deviation metrics of UV-Vis absorption spectra of ternary blended films with PM6 as donor and Y6, L8-BO, BTP-eC9, BO-4Cl as acceptors, respectively, and PC₆₁PeA as the third component, annealed for 5 min at different temperatures with respect to the as-cast (room temperature) conditions.



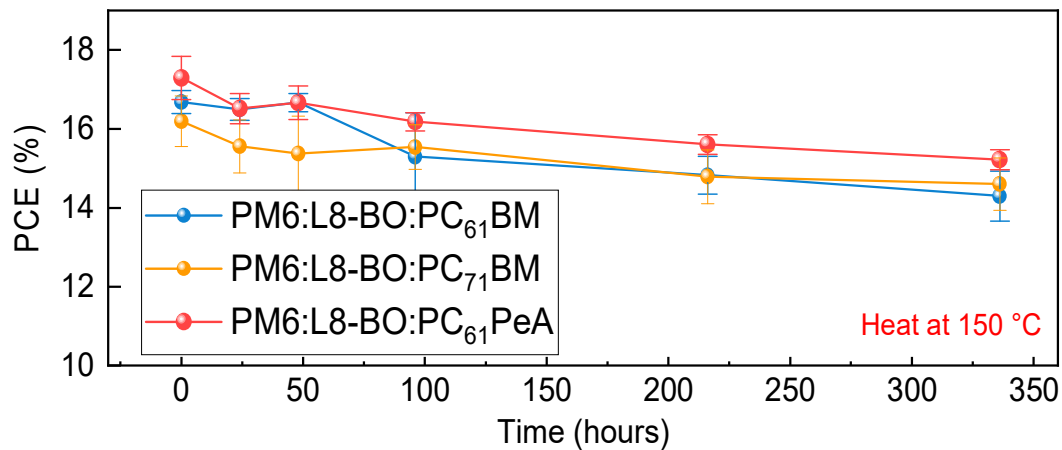
Supplementary Figure 8. Differentiate deviation metrics of UV-Vis absorption spectra of single-component films at different temperatures. Differentiation of the temperature-dependent curves of the deviation metrics of PM6, Y6, L8-BO, BTP-eC9, BO-4Cl and PC₆₁PeA films and the corresponding T_{onset} . The curves are obtained by segmented linear fitting.



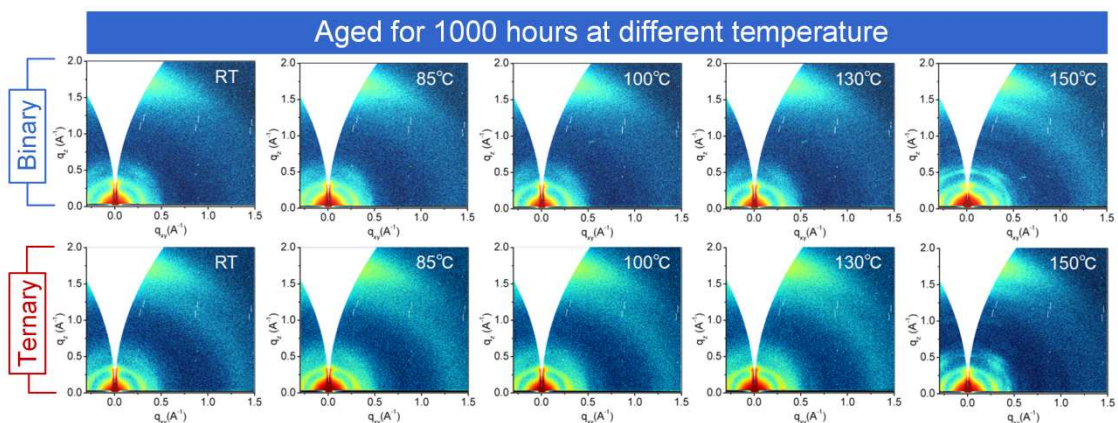
Supplementary Figure 9. Differentiate deviation metrics of UV-Vis absorption spectra of binary films at different temperatures. Differentiation of the temperature-dependent curves of the deviation metrics of binary blended films with PM6 as donor and Y6, L8-BO, BTP-eC9, BO-4Cl as acceptors, respectively, and the corresponding T_{onset} . The curves are obtained by segmented linear fitting.



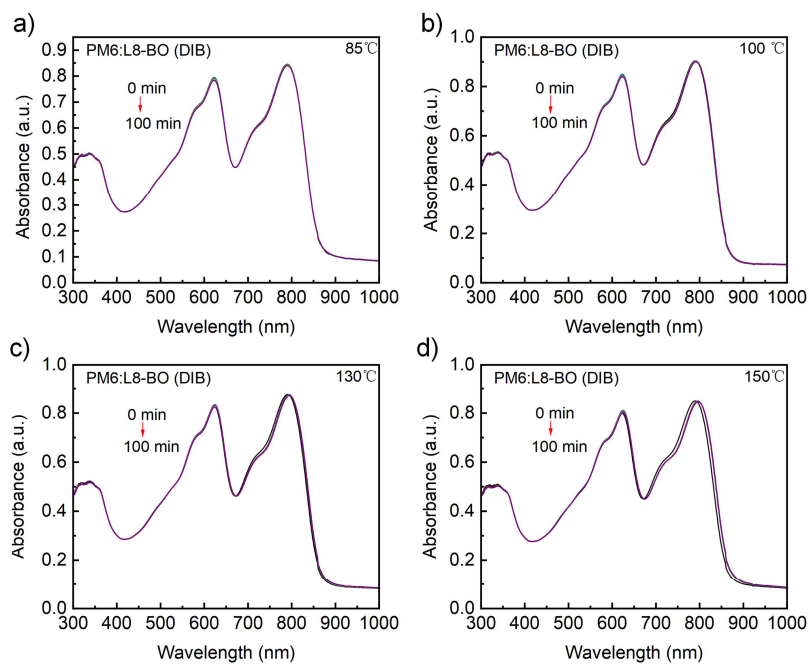
Supplementary Figure 10. Differentiate deviation metrics of UV-Vis absorption spectra of ternary films at different temperatures. Differentiation of the temperature-dependent curves of the deviation metrics of ternary blend films with PM6 as the donor, Y6, L8-BO, BTP-eC9, BO-4Cl as the acceptors, respectively, and PC₆₁PeA as the third component, and the corresponding T_{onset} . The curves are obtained by segmented linear fitting.



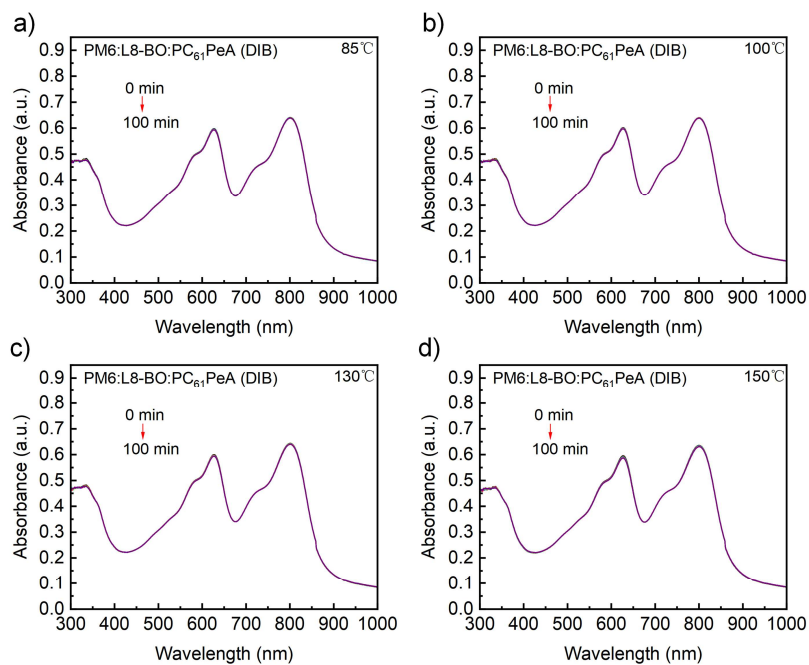
Supplementary Figure 11. Comparison of different fullerene doping. Efficiency of PM6:L8-BO system inverted OPVs doped with different fullerenes as the third component as a function of heating time. The centre of the error bar is defined as the average value and error bar is defined as the standard deviation, which is calculated from the statistical results of at least six individual devices.



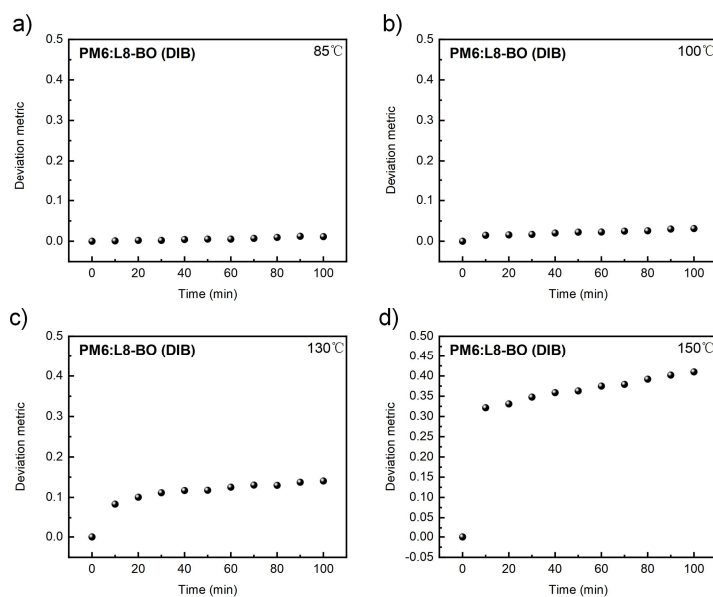
Supplementary Figure 12. GIWAX characterization of binary and ternary films annealed at different temperatures. 2D GIWAXS patterns of PM6:L8-BO and PM6:L8-BO:PC₆₁PeA blend films before and after 1,000 hours of annealing at different temperatures.



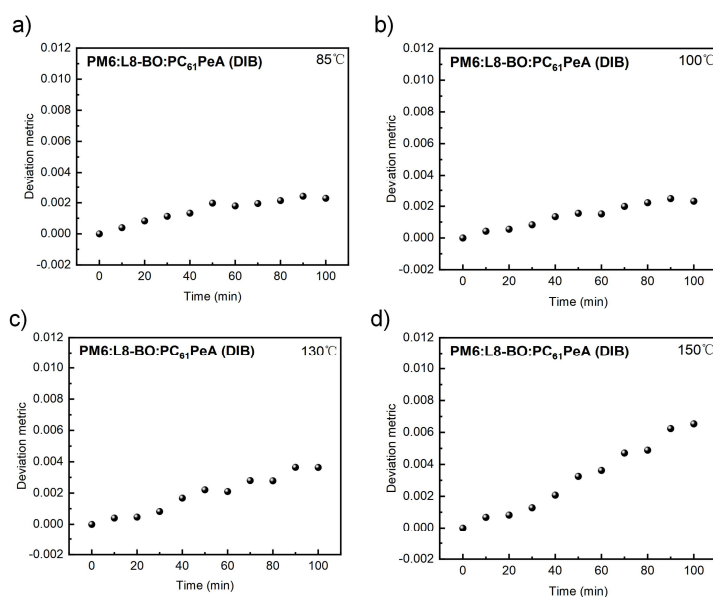
Supplementary Figure 13. UV-Vis absorption spectrum of binary films annealed at different temperatures. UV-Vis absorption spectra of binary blend films with PM6 as donor and L8-BO as acceptors, during annealing at different temperatures for 100 min.



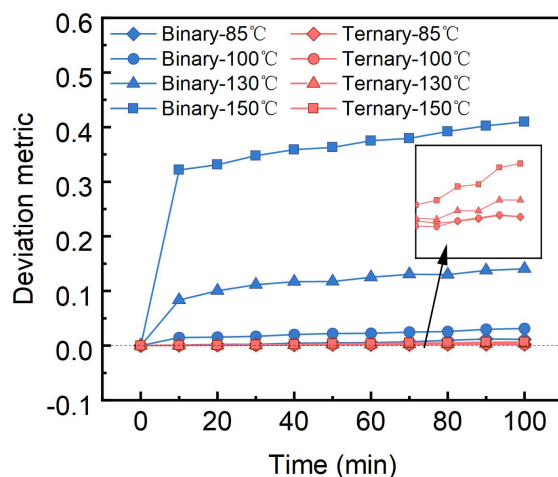
Supplementary Figure 14. UV-Vis absorption spectrum of ternary films annealed at different temperatures. UV-Vis absorption spectra of ternary blend films with PM6 as the donor, L8-BO as the acceptors, and PC₆₁PeA as the third component, during annealing at different temperatures for 100 min.



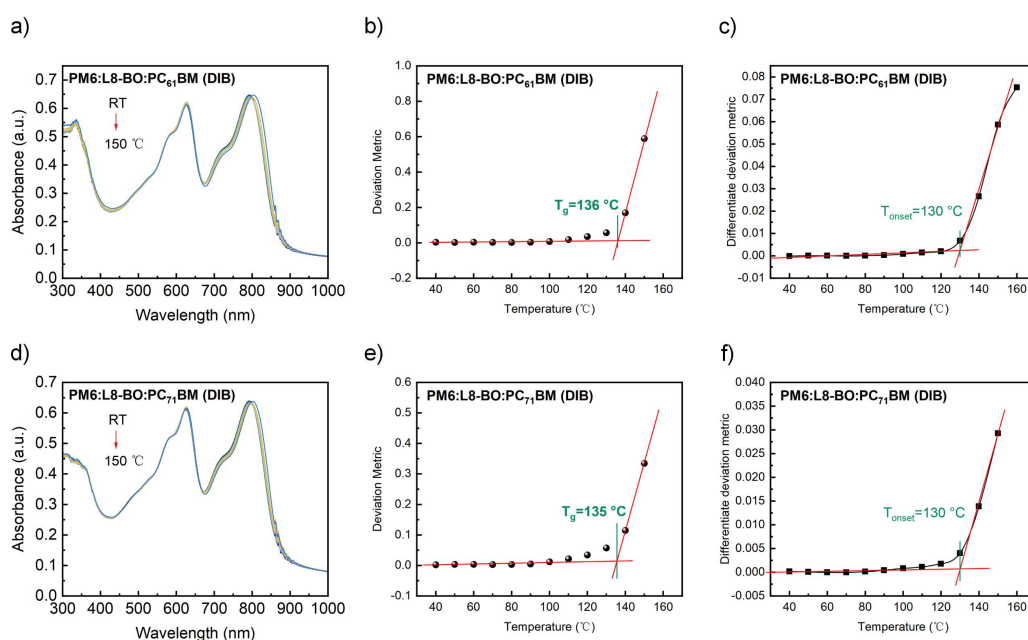
Supplementary Figure 15. Deviation metrics of UV-Vis absorption spectra of binary films annealed at different temperatures. Deviation metrics of UV-Vis absorption spectra of binary blended films with PM6 as donor and L8-BO as acceptors, during annealing at different temperatures for 100 min with respect to the as-cast (room temperature) conditions.



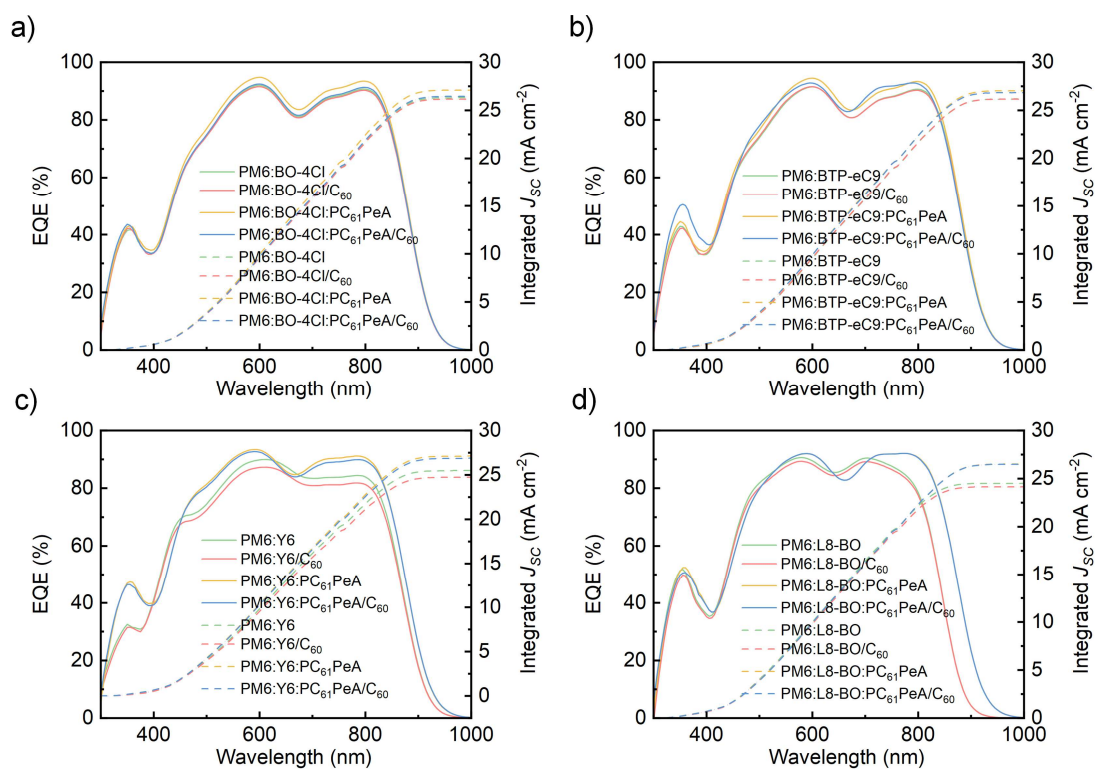
Supplementary Figure 16. Deviation metrics of UV-Vis absorption spectra of ternary films annealed at different temperatures. Deviation metrics of UV-Vis absorption spectra of ternary blend films with PM6 as the donor, L8-BO as the acceptors, and PC₆₁PeA as the third component, during annealing at different temperatures for 100 min with respect to the as-cast (room temperature) conditions.



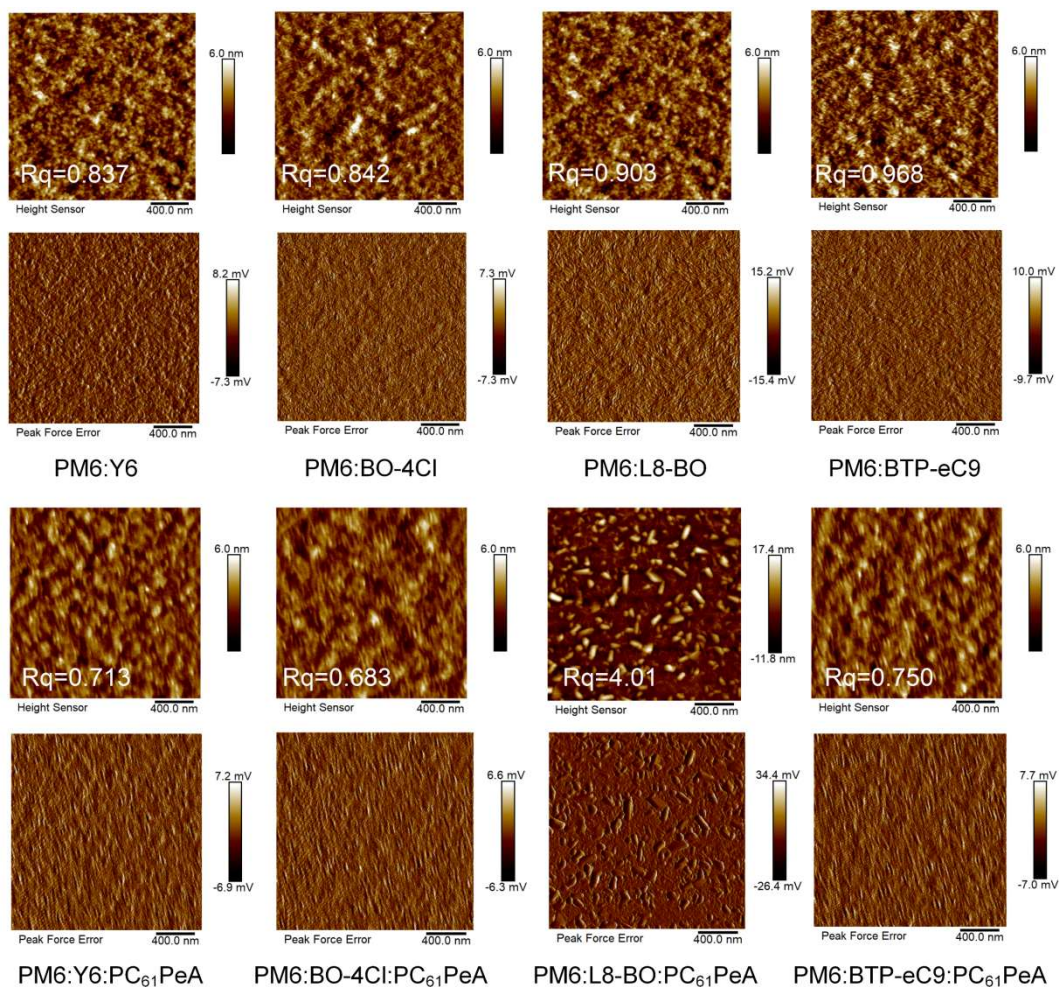
Supplementary Figure 17. Deviation metrics of UV-Vis absorption spectra of binary and ternary films annealed at different temperatures. Comparison of deviation metrics shift during annealing of binary and ternary blended films at different temperatures for 100 min with PM6 as donor, L8-BO as acceptor and PC₆₁PeA as the third component.



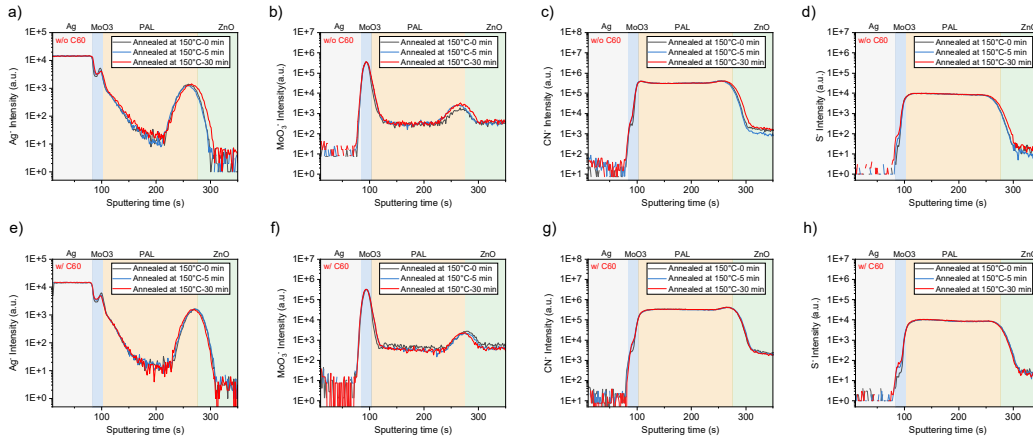
Supplementary Figure 18. UV-Vis absorption spectra, deviation metrics and differentiate deviation metrics of ternary films annealed at different temperatures. UV-vis absorption spectra, T_g and T_{onset} of PC₆₁BM and PC₇₁BM doped ternary blended films of PM6:L8-BO system. The curves are obtained by segmented linear fitting.



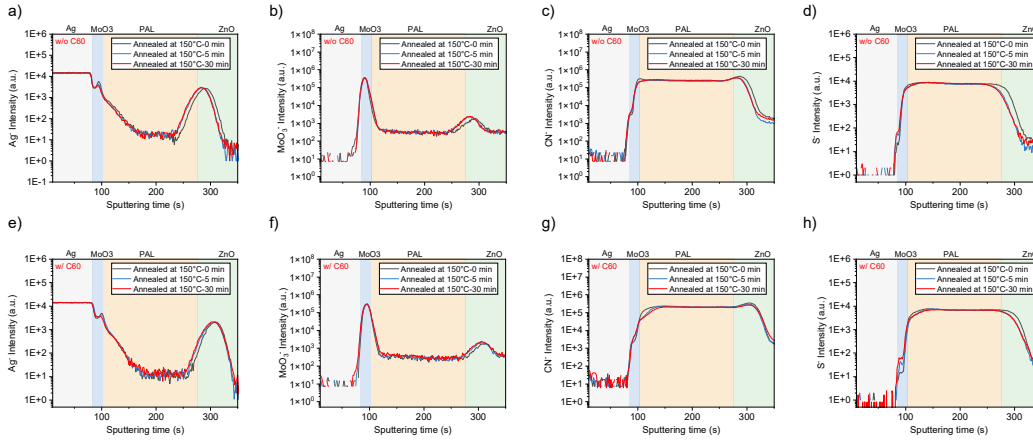
Supplementary Figure 19. EQE characterization of binary and ternary inverted organic solar cells. EQE curves and integration currents of binary and ternary inverted OPVs prepared with and without C_{60} using PM6 as donor, Y6, L8-BO, BTP-eC9, BO-4Cl as acceptors, respectively, and PC₆₁PeA as the third component.



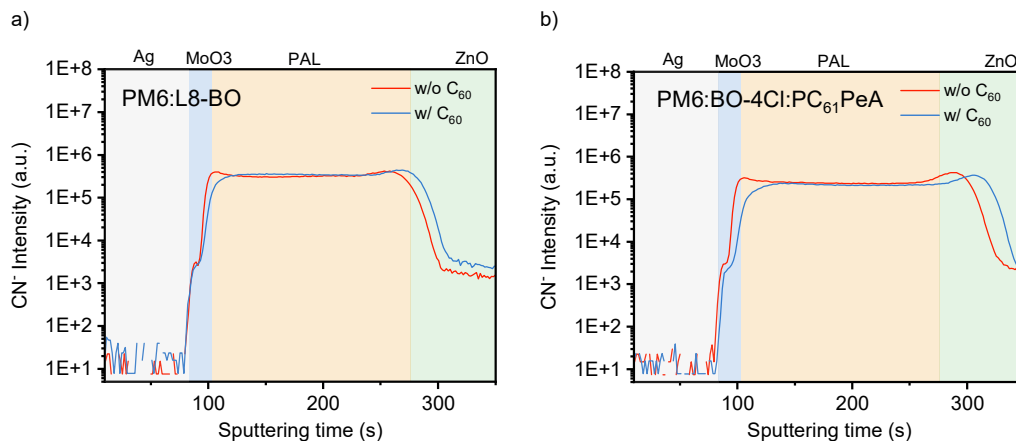
Supplementary Figure 20. AFM characterization of binary and ternary blend films. AFM images of binary and ternary blend films with PM6 as the donor, Y6, L8-BO, BTP-eC9, BO-4Cl as the acceptors, respectively, and PC₆₁PeA as the third component.



Supplementary Figure 21. TOF-SIMS characterization of binary devices with and without C₆₀. TOF-SIMS depth profiles of PM6:L8-BO-based devices prepared without (a-d) and with (e-h) a C₆₀ layer.



Supplementary Figure 22. TOF-SIMS characterization of ternary devices with and without C₆₀. TOF-SIMS depth profiles of PM6:BO-4Cl:PC₆₁PeA-based devices prepared without (a-d) and with (e-h) a C₆₀ layer.



Supplementary Figure 23. TOF-SIMS characterization of binary and ternary devices with and without C₆₀. TOF-SIMS depth profiles of CN⁻ for PM6:L8-BO -based device (a) and PM6:BO-4Cl:PC₆₁PeA-based device (b), prepared without and with a C₆₀ layer.



检测结果/说明:

Results of Test and additional explanation.

1. Standard Test Condition (STC): Total Irradiance: 1000 W/m²
Temperature: 25.0 °C
Spectral Distribution: AM1.5G

2.Measurement Data and I-V/P-V Curves under STC

Forward Scan

I_{sc} (mA)	V_{oc} (V)	I_{MPP} (mA)	V_{MPP} (V)	P_{MPP} (mW)	FF (%)	A (cm ²)
0.6917	0.8497	0.6383	0.7091	0.4526	77.01	0.0252

Reverse Scan

I_{sc} (mA)	V_{oc} (V)	I_{MPP} (mA)	V_{MPP} (V)	P_{MPP} (mW)	FF (%)	A (cm ²)
0.6923	0.8516	0.6398	0.7091	0.4537	76.96	0.0252

Mismatch factor:0.9927

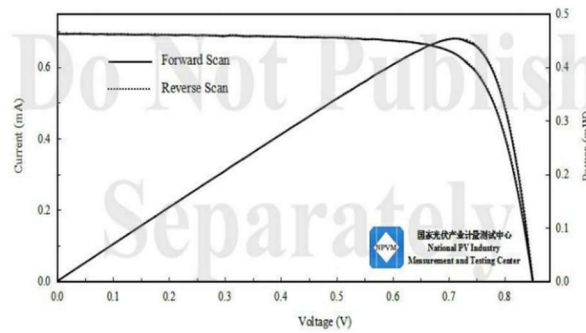


Figure 1. I-V and P-V characteristic curves of the measured sample under STC

Supplementary Figure 24. Efficiency certification. Optimised 0.0252 cm² ternary inverted organic solar cell efficiency certified by the National PV Industry Measurement and Testing Center (Fuzhou, China).



检测结果/说明:
Results of Test and additional explanation.

3.Measurement Data and Curves for MPPT under STC

η (%)	17.76
P_{MPP} (mW)	0.4475
I_{MPP} (mA)	0.6311
V_{MPP} (V)	0.7091

Note: Measurement data for MPPT under STC in the above table was the mean value acquired during the final 30 seconds of the 300 seconds test

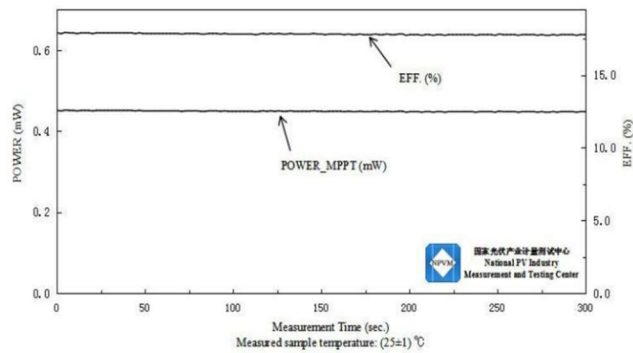
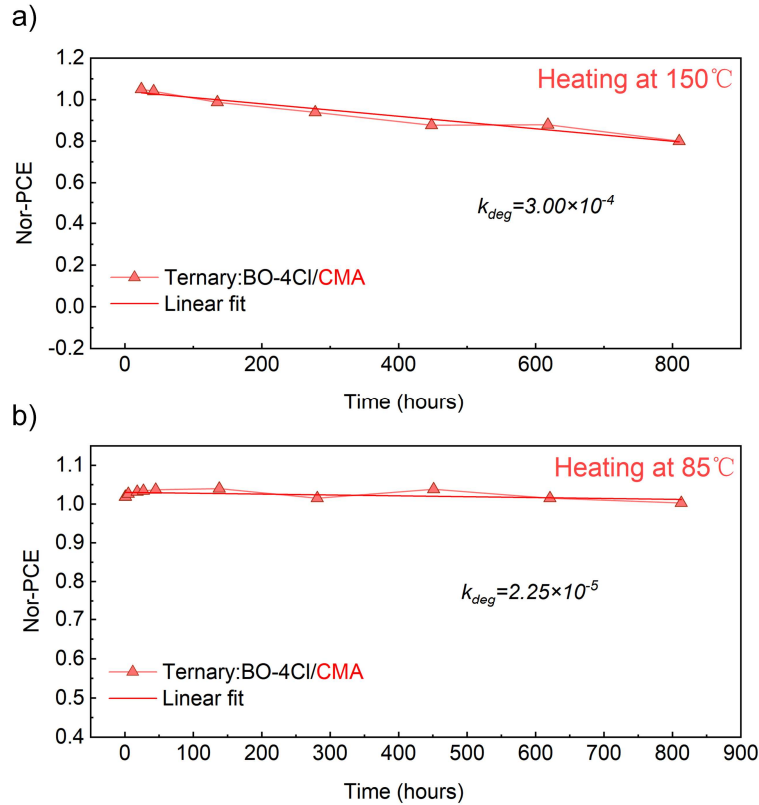
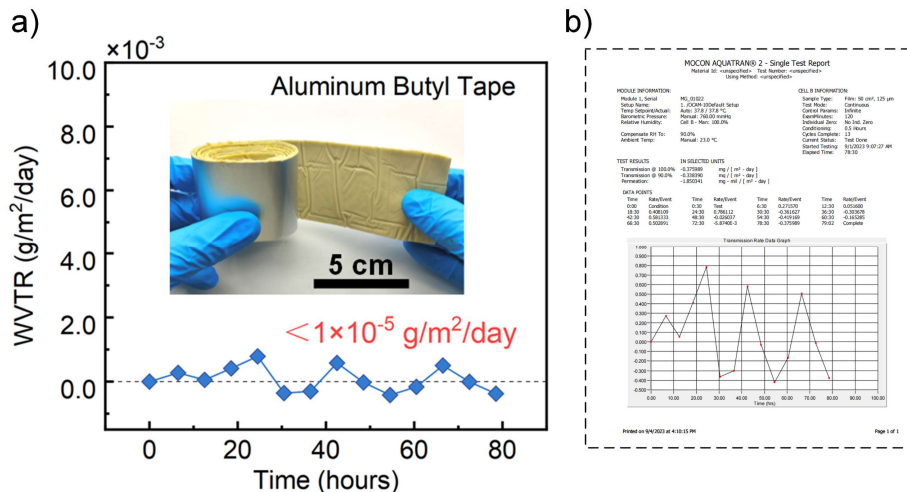


Figure 2. Measurement curves of the measured sample for MPPT

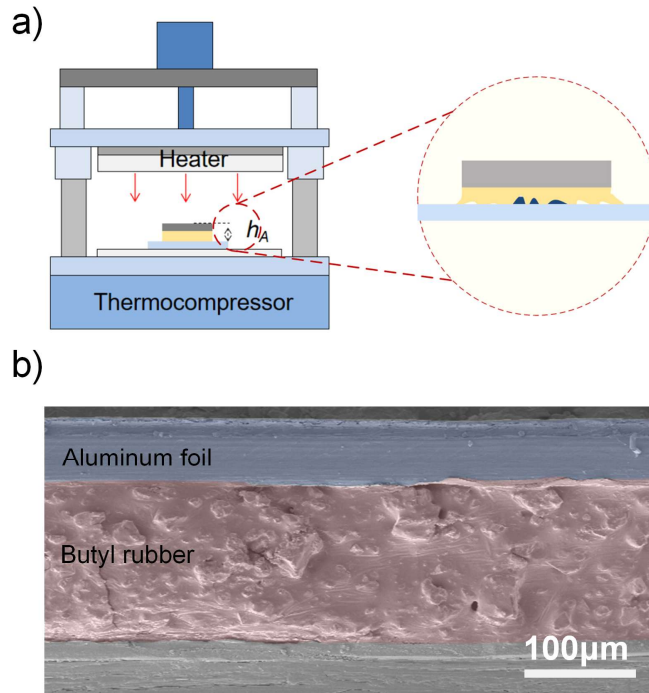
Supplementary Figure 25. Maximum power point tracking. The MPPT of optimised 0.0252 cm² ternary inverted organic solar cell efficiency certified by the National PV Industry Measurement and Testing Center (Fuzhou, China).



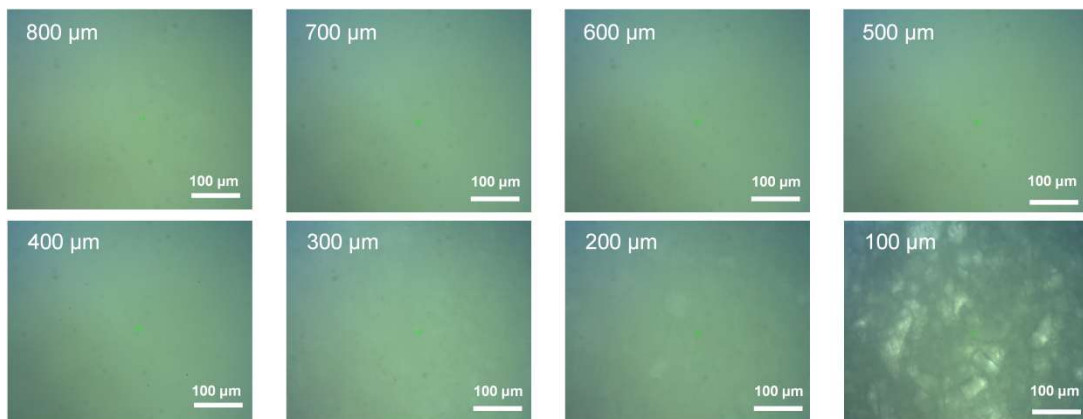
Supplementary Figure 26. Linear fitting of normalized efficiency degradation. Linear fitting of ternary inverted organic solar cells of PM6:BO-4Cl:PC₆₁PeA system with CMA structure at 150°C and 85°C thermal degradation. The initial initial device efficiency were 17.31% and 17.82%, respectively.



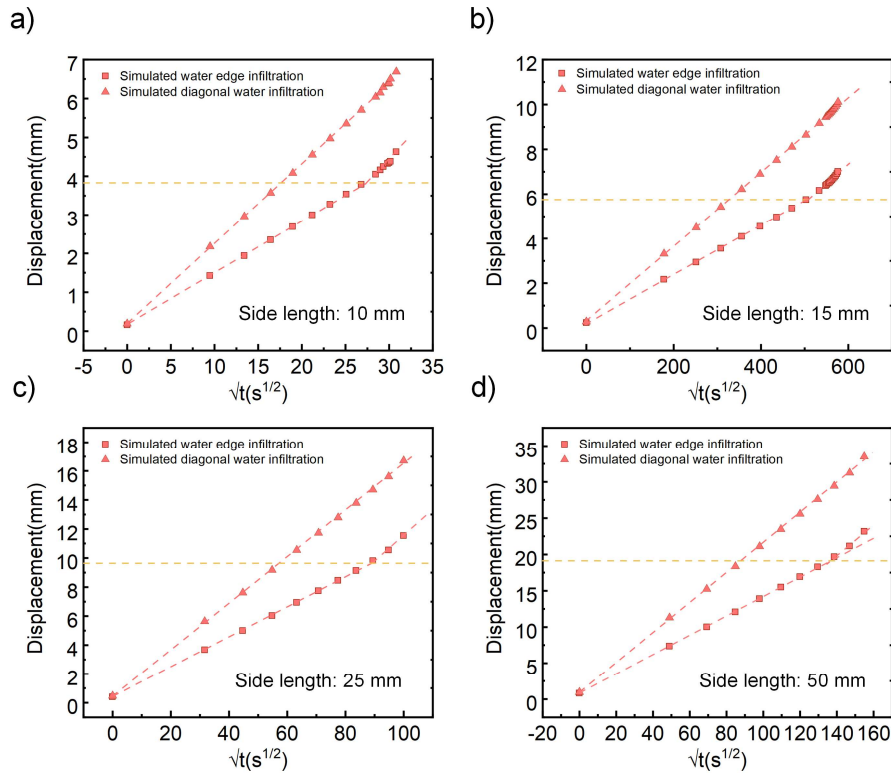
Supplementary Figure 27. Water vapor transmission rate characterization. The water vapor transmission rate (WVTR) of aluminium foil butyl tapes on the front side was tested by a water vapor transmission rate permeation analyzer (AQUATRAN MODEL 2, AMETEK MOCON) and the water content detected was below the test limit of the instrument.



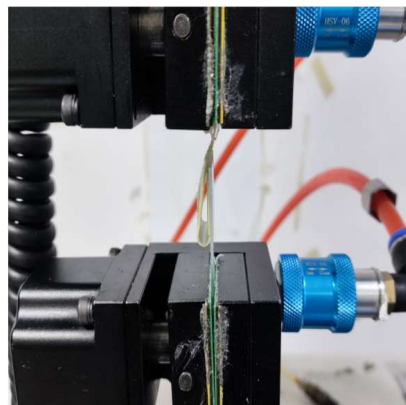
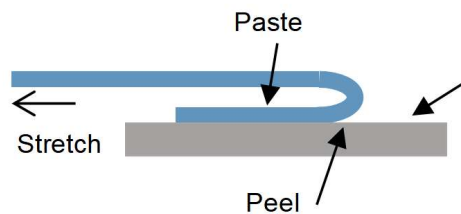
Supplementary Figure 28. Hot-press encapsulation. **a** Schematic diagram of hot-press encapsulation. **b** SEM cross-section of aluminium foil butyl tape attached to the substrate.



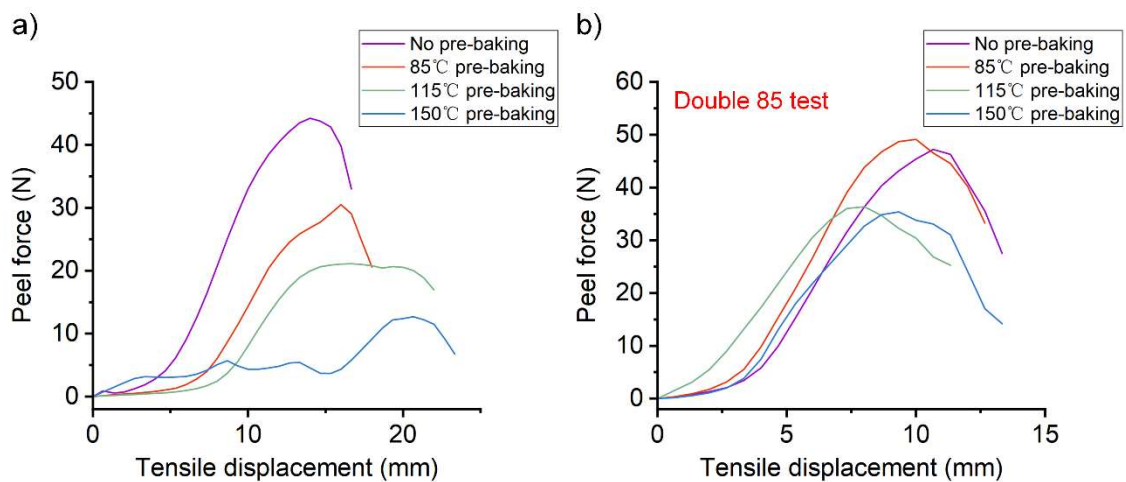
Supplementary Figure 29. Optical microscope characterization. Surface morphology of butyl rubbers of different thicknesses attached to a glass substrate as viewed through an optical microscope from the glass side. Significant fracture of the butyl rubber was observed at a thickness of 100 μm .



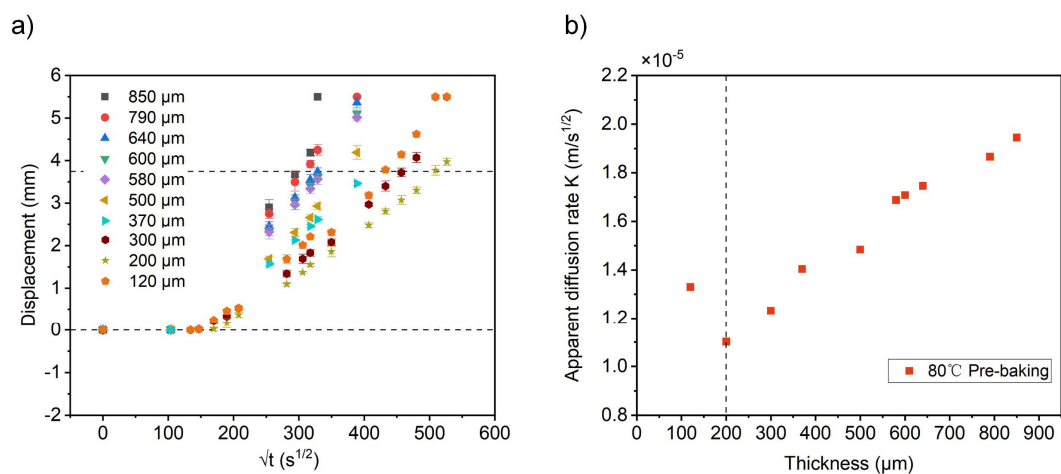
Supplementary Figure 30. Finite element simulation. Edge diffusion distance and diagonal diffusion distance versus diffusion time for different edge lengths and different water vapour diffusion rates based on finite element simulations. The curves are obtained by segmented linear fitting.



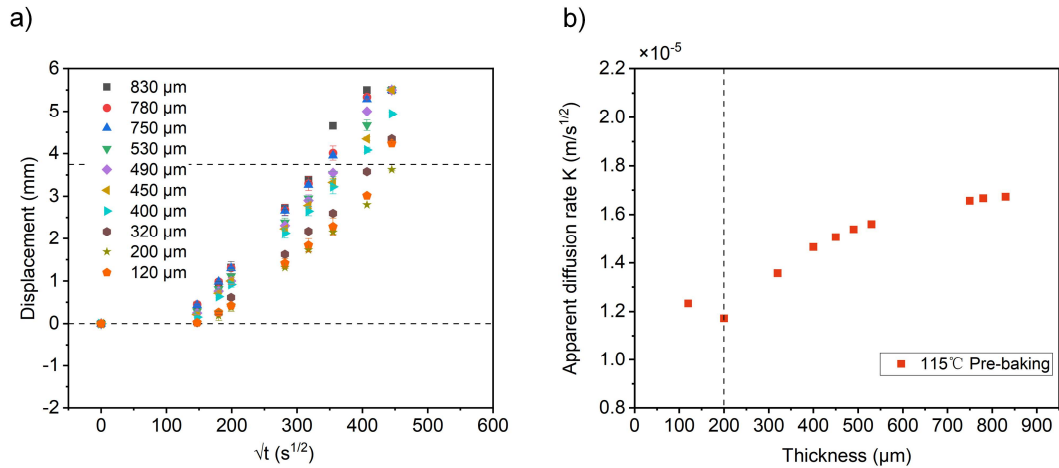
Supplementary Figure 31. Adhesion characterization. Schematic and photograph of tape adhesion test with 180° peel angle.



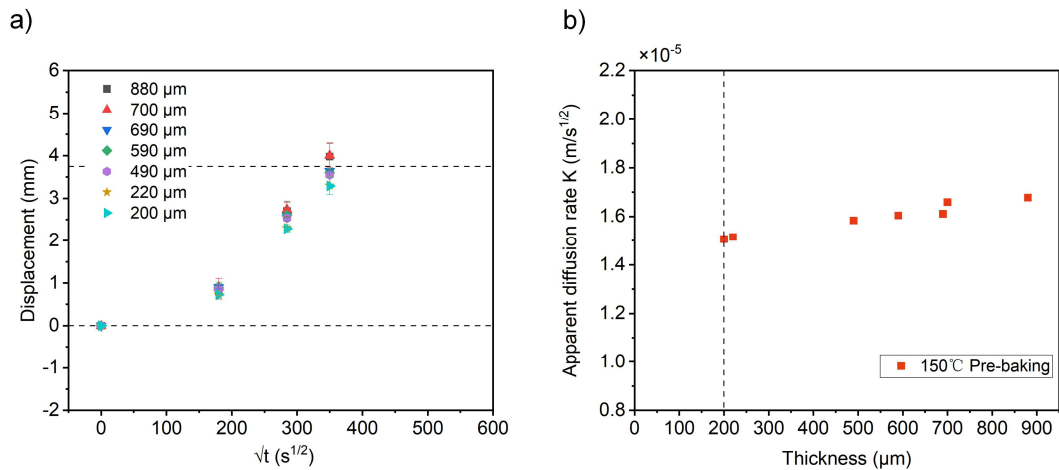
Supplementary Figure 32. Adhesion characterization. **a** Curves of peeling force and tensile displacement of adhesive tapes on substrates with different prebaking temperatures. **b** Curves of peeling force and tensile displacement of adhesive tapes after the double 85 test.



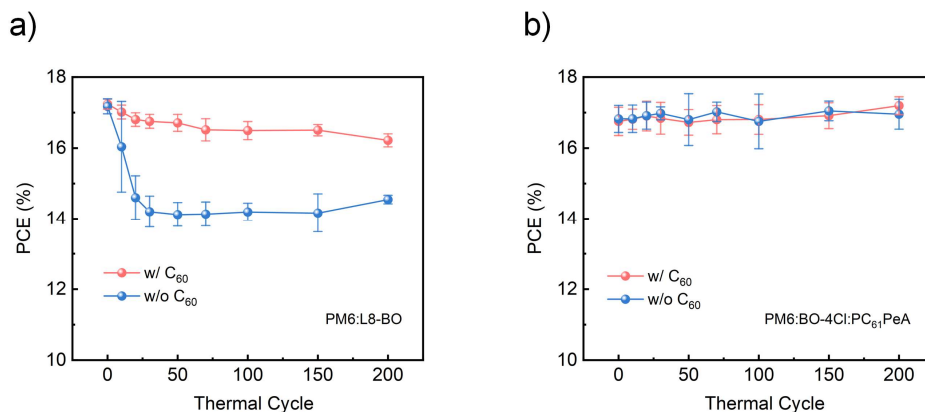
Supplementary Figure 33. Characterization of lateral diffusion of water vapor in 80°C prebaked encapsulant. **a** Relationship between edge corrosion distance and time for calcium films encapsulated with 80°C prebaked aluminium foil butyl tape encapsulants with different thicknesses of adhesive layers in the double 85 test. The centre of the error bar is defined as the average value and error bar is defined as the standard deviation, which is calculated from the statistical results of at least four data points. **b** Relationship between apparent diffusion rate K and adhesive layer thickness in 80°C prebaked aluminium foil butyl tape encapsulants encapsulation tests. Note that when the layer thickness is less than 200 μm, undesired cracks found within the films which explains the increased K value.



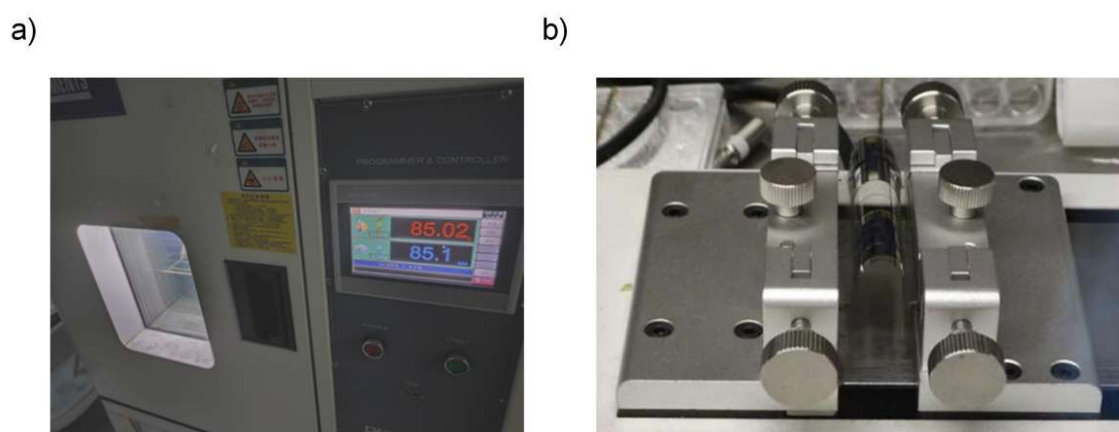
Supplementary Figure 34. Characterization of lateral diffusion of water vapor in 115°C prebaked encapsulant. **a** Relationship between edge corrosion distance and time for calcium films encapsulated with 115°C prebaked aluminium foil butyl tape encapsulants with different thicknesses of adhesive layers in the double 85 test. The centre of the error bar is defined as the average value and error bar is defined as the standard deviation, which is calculated from the statistical results of at least four data points. **b** Relationship between apparent penetration rate K and adhesive layer thickness in 115°C prebaked aluminium foil butyl tape encapsulants encapsulation tests.



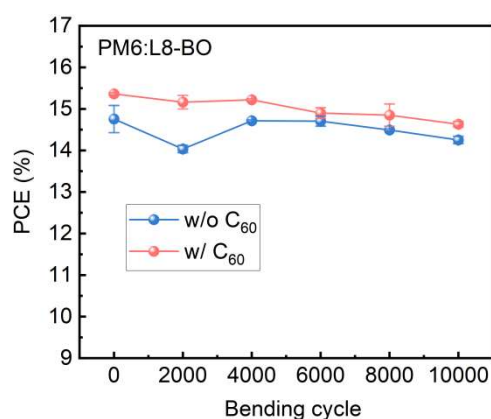
Supplementary Figure 35. Characterization of lateral diffusion of water vapor in 150°C prebaked encapsulant. **a** Relationship between edge corrosion distance and time for calcium films encapsulated with 150°C prebaked aluminium foil butyl tape encapsulants with different thicknesses of adhesive layers in the double 85 test. The centre of the error bar is defined as the average value and error bar is defined as the standard deviation, which is calculated from the statistical results of at least four data points. **b** Relationship between apparent penetration rate K and adhesive layer thickness in 150°C prebaked aluminium foil butyl tape encapsulants encapsulation tests.



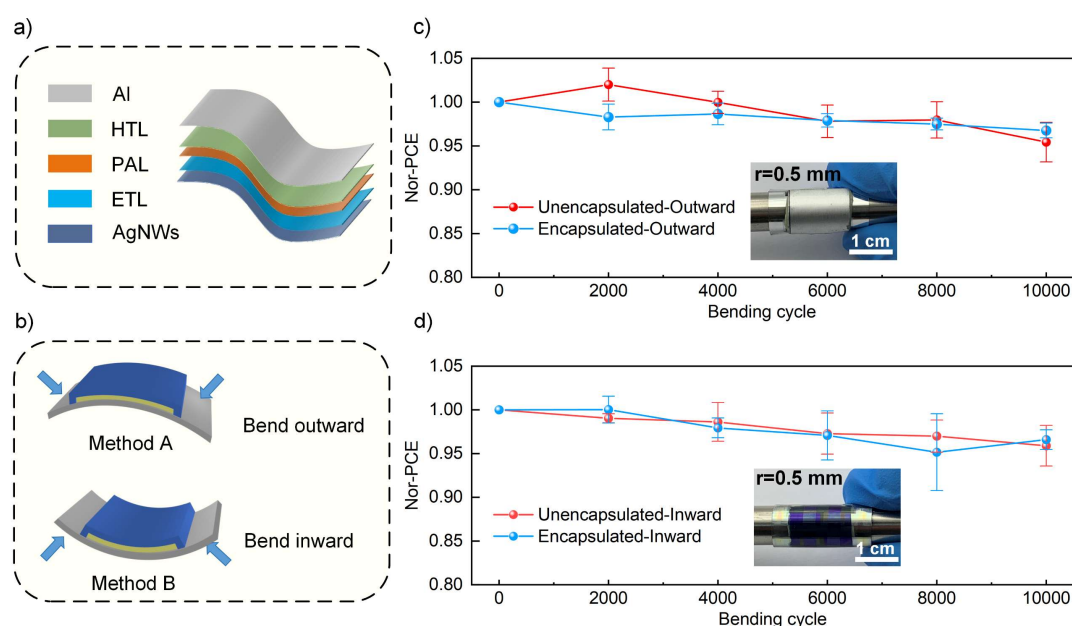
Supplementary Figure 36. Thermal cycling stability testing. **a** Efficiency versus cycle number curves of inverted OPVs with PM6:L8-BO system with and without C₆₀ interfacial layer during thermal cycling (-40°C-85°C). The centre of the error bar is defined as the average value and error bar is defined as the standard deviation, which is calculated from the statistical results of at least six individual devices. **b** Efficiency versus cycle number curves of inverted OPVs with PM6:BO-4Cl:PC₆₁PeA system with and without C₆₀ interfacial layer during thermal cycling (-40°C-85°C). The centre of the error bar is defined as the average value and error bar is defined as the standard deviation, which is calculated from the statistical results of at least ten individual devices.



Supplementary Figure 37. Damp heat, thermal cycling, and bending test equipment. Photos of climate chamber (D&R PVL-9001-16A, Suzhou D&R Instruments) for thermal cycling and damp heat tests (a) and bending machine (FlexTest-TM-L, Hunan) for bending tests (b).



Supplementary Figure 38. Bending test of devices with and without C₆₀. Efficiency degradation versus number of bends for flexible OPVs (PM6:L8-BO system) bent with or without C₆₀. The centre of the error bar is defined as the average value and error bar is defined as the standard deviation, which is calculated from the statistical results of six individual devices.



Supplementary Figure 39. Bending tests of encapsulated flexible devices. **a** Flexible organic solar cell structure (PM6:L8-BO system without C₆₀). **b** Schematic diagrams of outward and inward bending. **c-d** Curves of efficiency degradation versus the number of bends for flexible organic solar cells with or without encapsulation for outward (c) and inward bending. The centre of the error bar is defined as the average value and error bar is defined as the standard deviation, which is calculated from the statistical results of at least six individual devices.

Supplementary Tables

Supplementary Table 1. Summary of reported values of degradation activation energy of different types of solar cells.

Solar Cells	E_a (eV)	Efficiency decrease (Conditional; % hr ⁻¹)	Ref.
Silicon	0.95; 1.15	0.000042	3
GaAs	1.02	0.0000285	4
Perovskite	0.274; 0.3; 0.61; 0.634; 0.687; 0.725	0.06; 0.01; 0.02; 0.00416; 0.00167; 0.0005	5-8
Organic	0.35; 0.52*	0.0044; 0.0027; 0.0011; 0.00027*	⁵ *This work

Supplementary Table 2. Summary of reports on organic solar cells for double 85 testing.

Year	Materials	PCE (%)	Double 85 Stability	Ref.
2014	P3HT:PCBM	2.7%	T95 > 1000 h	9
2015	-	1.5%	T80 ≈ 200 h	10
2016	-	2.5%	T80 ≈ 300 h	11
2020	P3HT:PC ₆₁ BM	2.4%	T80 ≈ 10 h	12
2023	P3HT:PCBM	2.8%	T80 ≈ 95 h	13
2025	PM6:L8-BO	17.8%	T95 > 1000 h*	*This work

Supplementary Table 3. GIWAXS Characteristics of PM6:L8-BO and PM6:L8-BO:PC₆₁PeA blend films with the different stored conditions

Materials	Storage temperature	Peak	Location (Å ⁻¹)	D-spacing (Å)	FWHM (Å ⁻¹)	CCL (Å)
PM6:L8-BO	RT	(100) IP	0.304	20.685	0.065	86.426
		(010) OOP	1.726	3.640	0.367	15.425
	85°C	(101) IP	0.304	20.691	0.063	89.760
		(010) OOP	1.737	3.617	0.350	16.176
	100°C	(100) IP	0.306	20.551	0.059	96.155
		(010) OOP	1.736	3.620	0.352	16.043
	130°C	(101) IP	0.301	20.853	0.058	96.929
		(010) OOP	1.727	3.639	0.337	16.777
	150°C	(100) IP	0.303	20.726	0.051	110.880
		(010) OOP	1.753	3.585	0.329	17.182
PM6:L8-BO:PC ₆₁ PeA	RT	(101) IP	0.309	20.313	0.064	87.727
		(010) OOP	1.738	3.614	0.348	16.246
	85°C	(100) IP	0.307	20.469	0.063	89.320
		(010) OOP	1.728	3.636	0.347	16.306
	100°C	(101) IP	0.309	20.329	0.064	88.537
		(010) OOP	1.738	3.615	0.347	16.291
	130°C	(100) IP	0.307	20.458	0.060	94.028
		(010) OOP	1.741	3.608	0.344	16.440
	150°C	(101) IP	0.301	20.883	0.056	100.210
		(010) OOP	1.751	3.588	0.317	17.813

Supplementary Table 4. T_g and T_{onset} of single-component, binary and ternary active layer films extracted by UV-Vis spectroscopy testing.

Materials	T_g (°C)	T_{onset} (°C)
PM6	-	129
PC ₆₁ PeA	-	155
Y6	110	88
L8-BO	113	93
BO-4Cl	95	85
BTP-eC9	97	85
PM6:Y6	128	96
PM6:L8-BO	127	95
PM6:BO-4Cl	102	89
PM6:BTP-eC9	113	89
PM6:Y6:PC ₆₁ PeA	-	129
PM6:L8-BO:PC ₆₁ PeA	-	130
PM6:BO-4Cl:PC ₆₁ PeA	-	127
PM6:BTP-eC9:PC ₆₁ PeA	-	128

Supplementary Table 5. Summary of T_g reported in the literature for donor and acceptor materials.

Materials	T_g (°C)	Materials	T_g (°C)
PBDB-TF (PM6)	120 ¹⁴ ; 170-180 ¹⁵	BTP-C3-4F (N3)	82 ¹⁶
PPV	140 ¹⁷	BTP-eC7	85 ¹⁶
TQ1	100~110 ¹⁷	BTP-4F-C12	78 ¹⁶
P3HT	12 ¹⁸ ; 20 ¹⁹	BTP-eC9	75 ¹⁶ 175 ²⁰
PTB7-Th	130 ²¹	TYT	217 ²²
PTQ10	181 ²³	DYBO	179 ²⁴
PTzBI-dF	84 ²⁵	MYBO	80 ²⁴
PC ₇₁ BM	140 ¹⁴ 、160 ¹⁷	TDY- α	115 ²⁴
ITIC-Th	180 ¹⁴	TDY- β	106 ²⁴
PC ₆₁ BM:PC ₇₁ BM	125 ¹⁷	ITIC	180 ²⁶
PC ₆₁ BM	110-150 ¹⁷	ZCCF3	115 ²⁷
DP-BTP	126 ²⁸	CPDT-ICM	126 ¹⁹
N3	88 ²⁸	DYV	134 ²⁰
Tet-1	247 ²⁹	IEICO-4F	190 ³⁰
BTP-4F (Y6)	102 ¹⁶ ; 99 ³¹		

Supplementary Table 6. Summary of T_g and corresponding device efficiencies of active layer blend films reported in the literature.

Materials	T_g (°C)	PCE (%)	Materials	T_g (°C)	PCE(%)
TQ1:PC ₆₁ BM	110	4.9 ¹⁷	PM6:BTP-4F		15.2 ¹⁶
TQ1:PC ₇₁ BM	110; 160	7.0 ¹⁷	PM6:BTP-4F:PC ₇₁ BM		16.1 ¹⁶
TQ1:PC ₆₁ BM:PC ₇₁ BM	120	4.5 ¹⁷	PM6:Y6		15.7 ¹⁶
TQ1:C ₆₀ :C ₇₀	141	3.6 ¹⁷	PM6:BTP-4F-C12		16.4 ¹⁶
P3HT:PC ₆₁ BM	50		PM6:BTP-eC7		14.9 ¹⁶
PTB7:C ₆₀ :C ₇₀	224	6.0 ¹⁷	PM6:BTP-eC9		17.8 ¹⁶
P3HT:PC ₆₁ BM:ICBA		3.9 ¹⁷	PM6:BTP-eC11		17.3 ¹⁶
P3HT:PC ₆₁ BM:PC ₇₁ BM		2.4 ¹⁷	PM6:TYT		18.15 ²²
P3HT:PC ₆₁ BM:bis-PCBM		3.6 ¹⁷	PM6:DYBO		18.1 ²⁴
PTB7:ICBA:PC ₇₁ BM		8.8 ¹⁷	PM6:MYBO		17.1 ²⁴
PTB7-Th:ICBA:PC ₇₁ BM		10.2 ¹⁷	PM6:TDY- α		18.1 ³¹
PPBDTBT:PC ₇₁ BM:ITIC		10.4 ¹⁷	PM6:TDY- β		17.0 ³¹
PPBDTBT:PC ₇₁ BM:ITIC-Th		10.2 ¹⁷	PTB7-Th:PC ₇₁ BM	124	9.7 ²¹
PBQx-TCl:PY-IT:PY-IV	106.9	18.81 ³²	PTQ10:Y6		10.5 ²³
D18:N3:DP-BTP		19 ²⁸	Y6:TPIIC	110 ³³	
PM6:Tet-1		16.92 ²⁹	Y6:ZCCF3	110 ²⁷	
PM6:L8-BO:Tet-1		19.31 ²⁹	PM6:Y6		16.8 ²⁷
PM6:L8-BO		18.65 ²⁹	PM6:Y6:ZCCF3		18.5 ²⁷
PM6:BTP-C3-4F(N3)		15.9 ¹⁶	P3HT:CPDT-ICM		8.17 ¹⁹
PM6:BTP-C3-4F(N3):PC ₇₁ BM		16.7 ¹⁶	PM6:DYV		18.6 ²⁰

Supplementary Table 7. Performance parameters of PM6:L8-BO system inverted OPVs doped with different fullerenes as the third component.

Conditions	V_{oc} (V)	J_{sc} (mA/cm ²)	FF (%)	PCE (%)
PM6:L8-BO:PC ₆₁ BM	0.861 0.856±0.005	26.39 26.06±0.33	75.17 75.16±0.72	17.08 16.77±0.24
PM6:L8-BO:PC ₇₁ BM	0.849 0.842±0.004	26.39 26.54±0.22	75.42 75.06±0.37	16.91 16.78±0.13
PM6:L8-BO:PC ₆₁ PeA	0.849 0.851±0.002	27.41 26.91±0.52	77.77 76.76±0.68	18.09 17.57±0.35

Supplementary Table 8. Performance parameters of the various binary and ternary cells with and without C₆₀ protection layer.

Materials	C ₆₀	V _{OC} (V)	J _{sc} (mA/cm ²)	J _{cal.} (mA/cm ²)	FF (%)	PCE (%)
PM6:Y6	w/o	0.821	26.18	25.49	78.82	16.95
		0.815±0.004	26.17±0.21		78.43±0.35	16.72±0.21
PM6:Y6	w/	0.832	25.68	24.75	78.12	16.70
		0.820±0.007	25.81±0.30		77.61± 0.81	16.43±0.23
PM6:Y6:PC ₆₁ PeA	w/o	0.805	28.52	27.11	77.80	17.86
		0.800±0.005	28.45±0.41		76.95± 0.80	17.52±0.29
PM6:Y6:PC ₆₁ PeA	w/	0.804	27.44	26.87	78.44	17.31
		0.799±0.004	27.75±0.46		76.13± 1.49	16.87±0.31
PM6:L8-BO	w/o	0.872	25.71	24.52	78.94	17.70
		0.868± 0.005	25.52± 0.33		79.01±0.16	17.51±0.15
PM6:L8-BO	w/	0.868	25.08	24.15	79.34	17.27
		0.868±0.002	25.09±0.20		78.65±0.55	17.13±0.14
PM6:L8-BO:PC ₆₁ PeA	w/o	0.847	27.39	26.50	77.92	18.07
		0.837±0.007	27.08± 0.51		77.35±0.581	17.53±0.336
PM6:L8-BO:PC ₆₁ PeA	w/	0.842	26.89	26.48	77.59	17.57
		0.839±0.004	26.62±0.30		77.10±0.45	17.21±0.26
PM6:BO-4Cl	w/o	0.839	27.29	26.31	74.99	17.17
		0.835±0.003	26.61±0.27		74.77±0.88	16.61±0.24
PM6:BO-4Cl	w/	0.835	26.68	26.17	75.11	16.73
		0.834±0.002	25.97±0.43		75.63± 0.85	16.38±0.26
PM6:BO-4Cl:PC ₆₁ PeA	w/o	0.831	27.63	27.10	81.05	18.60
		0.821±0.005	28.10± 0.51		77.67±1.59	17.91±0.32
PM6:BO-4Cl:PC ₆₁ PeA	w/	0.833	27.50	26.45	80.89	18.53
		0.822±0.007	27.97± 0.56		77.81±2.33	17.89±0.41
PM6:BTP-eC9	w/o	0.832	27.39	26.18	75.49	17.19
		0.832±0.002	26.91±0.55		75.37±0.87	16.88±0.34
PM6:BTP-eC9	w/	0.838	26.89	26.17	75.75	17.06
		0.832±0.003	26.87±0.26		74.80±0.75	16.73±0.23
PM6:BTP-eC9:PC ₆₁ PeA	w/o	0.814	28.42	27.03	77.09	17.84
		0.810±0.003	28.41±0.37		76.40±0.94	17.58±0.17
PM6:BTP-eC9:PC ₆₁ PeA	w/	0.811	27.99	26.84	77.58	17.61
		0.809±0.002	27.88±0.41		76.56±0.83	17.27±0.19

Supplementary Table 9. Key parameters and their ratios for different edge lengths and different edge water vapor diffusion rates based on finite element simulations.

L (mm)	K_{edge} ($10^{-5}\text{m/s}^{1/2}$)	K_{diag} ($10^{-5}\text{m/s}^{1/2}$)	D_0 (mm)	K_{diag}/K_{edge}	D_0/L
10	13	20.53	3.83	1.54	38.3%
15	1.08	1.66	5.75	1.54	38.3%
25	10.29	15.88	9.63	1.54	38.5%
50	13.29	20.50	19.12	1.54	38.2%

Supplementary Table 10. Parameter values obtained by fitting the equations for the apparent diffusion rate K and the thickness of the adhesive layer.

Pre-baking temperature	C_{SA} (mol/m ³)	D_A (m ² /s)	C_{SiH_2}/D_I	Coefficient of Determination (R^2)
80°C	11.43	4.49×10^{-10}	3.39×10^{-8}	0.99
115°C	9.85	1.95×10^{-10}	6.73×10^{-8}	0.96
150°C	7.07	5.19×10^{-11}	8.71×10^{-8}	0.96

Supplementary Table 11. Statistics on the contribution of bulk diffusion and interface diffusion under different conditions.

Encapsulants	h_A (μm)	K ($\text{m/s}^{1/2}$)	Bulk diffusion	Interface diffusion
80°C pre-baking	850	1.95×10^{-5}	71.03%	28.97%
	790	1.87×10^{-5}	71.61%	28.39%
	640	1.75×10^{-5}	65.89%	34.11%
	600	1.71×10^{-5}	64.38%	35.62%
	580	1.69×10^{-5}	63.63%	36.37%
	500	1.48×10^{-5}	69.14%	30.86%
	370	1.40×10^{-5}	56.29%	43.71%
	300	1.23×10^{-5}	56.64%	43.36%
	200	1.10×10^{-5}	44.99%	55.01%
115°C pre-baking	830	1.67×10^{-5}	34.33%	65.67%
	780	1.67×10^{-5}	32.51%	67.49%
	750	1.66×10^{-5}	31.68%	68.32%
	530	1.56×10^{-5}	25.46%	74.54%
	490	1.54×10^{-5}	24.23%	75.77%
	450	1.51×10^{-5}	23.29%	76.71%
	400	1.47×10^{-5}	21.94%	78.06%
	320	1.36×10^{-5}	20.55%	79.45%
150°C pre-baking	880	1.68×10^{-5}	13.30%	86.70%
	700	1.66×10^{-5}	10.44%	89.56%
	690	1.61×10^{-5}	9.98%	90.02%
	590	1.60×10^{-5}	8.50%	91.50%
	490	1.58×10^{-5}	6.98%	93.02%
	220	1.52×10^{-5}	3.05%	96.95%
	200	1.51×10^{-5}	2.77%	97.23%

Supplementary Table 12. Performance parameters of inverted organic solar cells before and after different hot press temperatures. The encapsulated devices were tested after being left for 12 hours.

Hot-press temperature	Conditions	V_{oc} (V)	J_{sc} (mA/cm ²)	FF (%)	PCE (%)
RT	Before encapsulation	0.876±0.002	24.97±0.12	75.58±0.67	16.54±0.17
	After encapsulation	0.879±0.002	26.01±0.12	75.21±0.55	17.19±0.18
40°C	Before encapsulation	0.879±0.002	25.08±0.17	75.61±0.97	16.66±0.12
	After encapsulation	0.883±0.004	26.22±0.14	74.78±0.78	17.31±0.10
60°C	Before encapsulation	0.877±0.004	24.88±0.16	74.71±2.18	16.30±0.52
	After encapsulation	0.880±0.005	25.72±0.12	74.75±1.63	16.93±0.39
80°C	Before encapsulation	0.877±0.003	25.02±0.15	76.08±0.99	16.70±0.28
	After encapsulation	0.884±0.002	25.85±0.23	75.21±0.81	17.18±0.29
100°C	Before encapsulation	0.877±0.003	24.94±0.21	76.05±0.60	16.63±0.20
	After encapsulation	0.881±0.002	25.80±0.27	75.44±0.73	17.14±0.26

Supplementary Table 13. Performance parameters of inverted organic solar cells before and after thermal cycling and damp heat testing.

Conditions	V_{oc} (V)	J_{sc} (mA/cm ²)	FF (%)	PCE (%)
Before thermal cycling	0.883±0.002	25.18±0.18	77.49±0.44	17.24±0.14
After thermal cycling	0.849±0.003	26.34±0.17	73.96±0.76	16.54±0.19
Before damp heat	0.885±0.006	25.46±0.20	75.37±1.2	16.98±0.44
After damp heat	0.891±0.008	24.45±0.26	73.53±1.44	16.02±0.43

Supplementary Table 14. Performance parameters of flexible organic solar cells before and after bending tests.

Conditions	Conditions	V_{oc} (V)	J_{sc} (mA/cm²)	FF (%)	PCE (%)
Without	Before bending	0.866±0.003	23.76±0.22	71.73±1.87	14.76±0.33
	C ₆₀ After bending	0.865±0.001	23.12±0.18	71.28±0.53	14.25±0.09
With	Before bending	0.872±0.004	23.67±0.24	74.42±0.87	15.36±0.03
	C ₆₀ After bending	0.864±0.003	23.62±0.05	71.66±0.54	14.63±0.07

Supplementary References

- 1 Root, S. E., Alkhadra, M. A., Rodriguez, D., Printz, A. D. & Lipomi, D. J. Measuring the Glass Transition Temperature of Conjugated Polymer Films with Ultraviolet–Visible Spectroscopy. *Chem. Mater.* **29**, 2646-2654 (2017).
- 2 Adams, J. *et al.* Water Ingress in Encapsulated Inverted Organic Solar Cells: Correlating Infrared Imaging and Photovoltaic Performance. *Adv. Energy Mater.* **5**, 1501065 (2015).
- 3 Cheng, X., Marstein, E. S., Haug, H., You, C. C. & Di Sabatino, M. Thermal stability of hydrogenated amorphous silicon passivation for p-type crystalline silicon. *Phys. Status. Solidi. (a)* **213**, 91-95 (2015).
- 4 Núñez, N., González, J. R., Vázquez, M., Algora, C. & Espinet, P. Evaluation of the reliability of high concentrator GaAs solar cells by means of temperature accelerated aging tests. *Prog. Photovolt: Res. Appl.* **21**, 1104-1113 (2012).
- 5 Khadka, D. B., Shirai, Y., Yanagida, M., Uto, K. & Miyano, K. Analysis of degradation kinetics of halide perovskite solar cells induced by light and heat stress. *Sol. Energy Mater. Sol. Cells* **246**, 111899 (2022).
- 6 Kim, J. *et al.* An effective method of predicting perovskite solar cell lifetime—Case study on planar CH₃NH₃PbI₃ and HC(NH₂)₂PbI₃ perovskite solar cells and hole transfer materials of spiro-OMeTAD and PTAA. *Sol. Energy Mater. Sol. Cells* **162**, 41-46 (2017).
- 7 Ma, Y. *et al.* Understanding Microstructural Development of Perovskite Crystallization for High Performance Solar Cells. *Adv. Mater.* **35**, 2306947 (2023).
- 8 Zhao, X. *et al.* Operationally stable perovskite solar modules enabled by vapor-phase fluoride treatment. *Science* **385**, 433-438 (2024).
- 9 Sapkota, S. B., Spies, A., Zimmermann, B., Dürr, I. & Würfel, U. Promising long-term stability of encapsulated ITO-free bulk-heterojunction organic solar cells under different aging conditions. *Sol. Energy Mater. Sol. Cells* **130**, 144-150 (2014).
- 10 Kim, S. H., Son, H. J., Park, S. H., Hahn, J. S. & Kim, D. H. A study for degradation of flexible organic photovoltaic modules via damp-heat test: By accessing individual layers of the module. *Sol. Energy Mater. Sol. Cells* **144**, 187-193 (2016).
- 11 Son, H. J., Kim, S. H. & Kim, D. H. Critical Impact of Hole Transporting Layers and Back Electrode on the Stability of Flexible Organic Photovoltaic Module. *Adv. Energy Mater.* **7**, 1601289 (2016).
- 12 Planes, E. *et al.* Encapsulation Effect on Performance and Stability of Organic Solar Cells. *Adv. Mater. Interfaces* **7**, 2000293 (2020).
- 13 Wachsmuth, J. *et al.* Overcoming Moisture-Induced Degradation in Organic Solar Cells. *Adv. Eng. Mater.* **25**, 2300595 (2023).
- 14 Lee, C. *et al.* Novel Diffusion-Regulated Layering Methodology to Improve Blend Miscibility and Thermal Stability of Organic Photovoltaics. *Adv. Funct. Mater.* **34**, 2308047 (2023).
- 15 Guan, C. *et al.* Non-Covalent Interactions between Polyvinyl Chloride and Conjugated Polymers Enable Excellent Mechanical Properties and High Stability in Organic Solar Cells. *Angew. Chem. Int. Ed.* **62**, e202312357 (2023).
- 16 Qin, Y. *et al.* The performance-stability conundrum of BTP-based organic solar cells. *Joule* **5**, 2129-2147 (2021).
- 17 de Zerio, A. D. & Müller, C. Glass Forming Acceptor Alloys for Highly Efficient and Thermally Stable Ternary Organic Solar Cells. *Adv. Energy Mater.* **8**, 1702741 (2018).

- 18 Munshi, J., Chien, T., Chen, W. & Balasubramanian, G. Elasto-morphology of P3HT:PCBM
bulk heterojunction organic solar cells. *Soft Matter* **16**, 6743-6751 (2020).
- 19 Han, D. *et al.* Efficient, thermally stable poly(3-hexylthiophene)-based organic solar cells
achieved by non-covalently fused-ring small molecule acceptors. *J. Mater. Chem. A* **10**, 640-
650 (2022).
- 20 Wan, J. *et al.* Enabling Highly Efficient and Thermal-Stable Polymer Solar Cells through
Semi-Alloy Acceptors Composed of a Hinge-Like Dimer: A Versatile Doping Protocol. *Adv.*
Mater. **35**, 2302592 (2023).
- 21 Yin, J. *et al.* Improved Glass Transition Temperature towards Thermal Stability via Thiols
Solvent Additive versus DIO in Polymer Solar Cells. *Macromol. Rapid Commun.* **38**, 1700428
(2017).
- 22 Lee, J.-W. *et al.* Trimerized small-molecule acceptors enable high-performance organic solar
cells with high open-circuit voltage and prolonged life-time. *Energy Environ. Sci.* **16**, 3339-
3349 (2023).
- 23 Riera-Galindo, S. *et al.* High Polymer Molecular Weight Yields Solar Cells with
Simultaneously Improved Performance and Thermal Stability. *Small* **20**, 2311735 (2024).
- 24 Sun, C. *et al.* Dimerized small-molecule acceptors enable efficient and stable organic solar
cells. *Joule* **7**, 416-430 (2023).
- 25 Fan, B., Gao, H. & Jen, A. K. Y. Biaxially Conjugated Materials for Organic Solar Cells. *ACS*
Nano **18**, 136-154 (2023).
- 26 Yu, L. *et al.* Diffusion-Limited Crystallization: A Rationale for the Thermal Stability of Non-
Fullerene Solar Cells. *ACS Appl. Mater. Interfaces* **11**, 21766-21774 (2019).
- 27 Zhang, C. *et al.* Diffusion-Limited Acceptor Alloy Enables Highly Efficient and Stable
Organic Solar Cells. *Adv. Funct. Mater.* **33**, 2214392 (2023).
- 28 Liu, X. *et al.* A Pyrene-Fused Dimerized Acceptor for Ternary Organic Solar Cells with 19%
Efficiency and High Thermal Stability. *Angew. Chem. Int. Ed.* **63**, e202316039 (2023).
- 29 Zhang, C. *et al.* Simple and Efficient Synthesis of Novel Tetramers with Enhanced Glass
Transition Temperature for High-Performance and Stable Organic Solar Cells. *Angew. Chem.*
Int. Ed. **63**, e202316295 (2023).
- 30 Armin, A. *et al.* A History and Perspective of Non-Fullerene Electron Acceptors for Organic
Solar Cells. *Adv. Energy Mater.* **11**, 2003570 (2021).
- 31 Bai, Y. *et al.* Geometry design of tethered small-molecule acceptor enables highly stable and
efficient polymer solar cells. *Nat. Commun.* **14**, 2926 (2023).
- 32 Ma, R. *et al.* Tunable Donor Aggregation Dominance in a Ternary Matrix of All-Polymer
Blends with Improved Efficiency and Stability. *Adv. Mater.* **36**, 2304632 (2024).
- 33 Wan, J. *et al.* High-performance ternary solar cells by introducing a medium bandgap acceptor
with complementary absorption, reducing energy disorder and enhancing glass transition
temperature. *J. Mater. Chem. A* **10**, 17122-17131 (2022).